HHS Public Access

Author manuscript

J Med Chem. Author manuscript; available in PMC 2018 September 10.

Published in final edited form as:

J Med Chem. 2018 August 23; 61(16): 7116–7130. doi:10.1021/acs.jmedchem.8b00253.

Molecular Imaging of Sirtuin1 Expression−Activity in Rat Brain Using Positron-Emission Tomography−Magnetic-Resonance Imaging with [^{18}F]-2-Fluorobenzoylaminohexanoicanilide

Robin Bonomi[†,‡], **Vadim Popov**[†,‡,□], **Maxwell T. Laws**[†,‡], **David Gelovani**[†,‡], **Anjoy Majhi**[†,‡,¶], **Aleksandr Shavrin**[†,‡], **Xin Lu**[‡,§], **Otto Muzik**[‡,§], **Nashaat Turkman**[†,‡,⊥], **Renshyan Liu**[‖], **Thomas Mangner**[‡,§], and **Juri G. Gelovani**[*,†,‡]

[†]Karmanos Cancer Institute, Detroit, Michigan 48202, United States

[‡]Departments of Biomedical Engineering, Oncology, and Neurosurgery, Detroit, Michigan 48202, United States

[§]Cyclotron/Radiochemistry Facility, Wayne State University, Detroit, Michigan 48202, United States

[‖]National Taiwan University, Taipei City 10617, Taiwan

Abstract

Sirtuin 1 (SIRT1) is a class III histone deacetylase that plays significant roles in the regulation of lifespan, metabolism, memory, and circadian rhythms and in the mechanisms of many diseases. However, methods of monitoring the pharmacodynamics of SIRT1-targeted drugs are limited to blood sampling because of the invasive nature of biopsies. For the noninvasive monitoring of the spatial and temporal dynamics of SIRT1 expression−activity in vivo by PET−CT−MRI, we developed a novel substrate-type radio-tracer, [^{18}F]-2-fluorobenzoylaminohexanoicanilide (2-[^{18}F]-BzAHA). PET−CT−MRI studies in rats demonstrated increased accumulation of 2-[^{18}F]BzAHA-derived radioactivity in the hypothalamus, hippocampus, nucleus accumbens, and locus coeruleus, consistent with autoradiographic and immunofluorescent (IMF) analyses of brain-tissue sections. Pretreatment with the SIRT1 specific inhibitor, EX-527 (5 mg/kg, ip), resulted in about a 20% reduction of 2-[^{18}F]BzAHA-derived-radioactivity accumulation in these structures. In vivo imaging of SIRT1 expression−activity should facilitate studies that improve the

[*]Corresponding Author: Tel.: 313-577-1271. juri.gelovani@wayne.edu.

[⊥]N.T.: University of Stony Brook Cancer Center, New York, NY 11794, United States. nashaat.turkman@stonybrookmedicine.edu.

[¶]A.M.: Presidency University, Kolkata 700073, India. anjoy.chem@presiuniv.ac.in.

[□]V.P.: Nanotechnology Education and Research Center, South Ural State University, Chelyabinsk 454080, Russia. popov.ioc@gmail.com.

Author Contributions

J.G.G. designed the studies; R.B., V.P., A.M., and N.T. performed the chemical syntheses; R.B., N.T., and T.M. performed the radiolabeling; A.S. performed the enzyme assays; R.B., M.T.L., X.L., and O.M. performed the in vivo imaging studies; D.J.G. performed immunohistochemistry; R.B., M.T.L., D.G., and A.S. analyzed and interpreted the data; and R.B., R.S.L., and J.G.G. wrote the manuscript.

The authors declare no competing financial interest.

ASSOCIATED CONTENT The Supporting Information is available free of charge on the ACS Publications website at DOI: 10.1021/acs.jmedchem.8b00253. Additional NMR data, PET−MR images, image quantification, and other fluorescence-microscopy images (PDF) Molecular-formula strings (CSV)

understanding of SIRT1-mediated regulation in the brain and aid in the development and clinical translation of SIRT1-targeted therapies.

Abstract

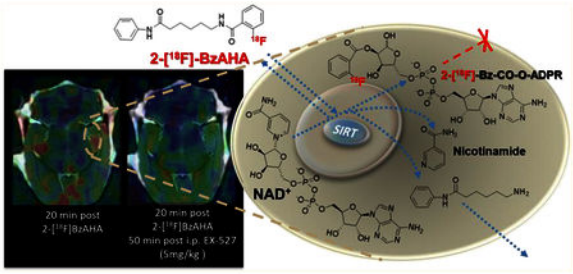

INTRODUCTION

Class III HDAC enzymes are termed silent information regulators or sirtuins (SIRTs), first discovered as the yeast Sir2 homologue, and are Zn^{2+}-independent but NAD^{+}-dependent.[1] Seven isotypes of SIRTs (SIRT1−7) have been identified in humans and other mammals.[2] These enzymes play important roles in the epigenetic regulation of gene expression, the cell cycle, metabolism, apoptosis, life span,[3] and circadian rhythms.[4] In particular, SIRT1 has been recognized as a key regulator of several molecular pathways that are important in the development and progression of cancer,[5] diabetes,[6] and cardiovascular[7] and neurological diseases.[8] SIRT1 shuttles between the cell nucleus and cytoplasm and deacetylates both histone proteins, such as H3K9, H3K14, and H4K16, and multiple nonhistone proteins, including PPARγ, NF-Kβ, members of the p53 family of proteins, and others.[9]

Because of the biological importance of SIRT1, several small-molecule activators and inhibitors of SIRT1 have been developed and tested for therapies for various diseases. For example, resveratrol, a natural activator of SIRT1, and SRT2104, a synthetic activator, have undergone clinical trials for the treatment of diabetes and obesity.[10] Because of the widely recognized role of SIRT1 in cancer, several SIRT1 inhibitors, including Selisistat (EX-527),[11] Sirtinol,[12] and Tenovin-6,[13] have been tested as therapies for various malignancies.[14] Also, SIRT1-targeted drugs have been tested for the treatment of various neurodegenerative diseases.[15] However, methods for monitoring the pharmacodynamics of SIRT1-specific activators and inhibitors are limited because of unacceptable traumatism from invasive biopsies, especially in CNS. Therefore, in most clinical trials, the pharmacodynamics of various SIRT1-targeted drugs has been monitored by measuring SIRT1 activity in blood mononuclear cells or in muscle- or liver-tissue biopsies.[16] Although measurements of SIRT1 mRNA- or protein-expression levels in fixed tissues reflect the levels of SIRT1 expression, these methods do not provide information about SIRT1 enzyme activity. Further-more, measurements of SIRT1 enzyme activity in tissue lysates are performed under biochemically optimized conditions and do not accurately reflect the SIRT1 enzyme activity in organs and tissues in vivo because of differences in intracellular NAD^{+} levels and the absence of other factors that influence the enzymatic activity of SIRT1. Therefore, we aimed to develop a noninvasive and quantitative in vivo imaging method using a SIRT1-specific substrate-type

radiotracer, which should provide valuable information about SIRT1 expression−activity levels in different organs and tissues under physiological or pathological conditions. Moreover, such an in vivo imaging methodology should provide the means for the noninvasive monitoring of the pharmacodynamics of novel SIRT1 activators and inhibitors and facilitate their translation into the clinic.

Our approach to the development of a SIRT1-specific substrate-type radiotracer for PET imaging was based on a well-established catalytic mechanism of SIRT1 for various endogenous and artificial substrates.[17] Previously, we successfully used this approach for the development of the HDAC class IIa specific substrate-type radiotracers [^{18}F]FAHA[18] and [^{18}F]TFAHA.[19] The current approach was based on previous reports demonstrating that SIRT1 is able to cleave large aromatic chemical groups, such as phenylacetyl,[20] from the ε-amine of lysine. Although other SIRT enzymes can cleave long acyl chains from lysine, they are not capable of cleaving aromatic-ring-containing moieties.[20] On the basis of these reports, we synthesized a focused library of 10 compounds in which the ε-amine of lysine was derivatized with aromatic-ring-containing moieties (with or without halogen substitutions), determined their substrate efficiencies for SIRT1−7, and established structure −activity relationships (SAR). As the result, we selected a 2-fluorobenzoyl-substituted lysine analogue for further radiolabeling with F-18 and in vivo imaging studies. The lead compound, [^{18}F]-2-fluorobenzoylaminohexanoicanilide (2-[^{18}F]BzAHA), demonstrated efficacy for PET−CT−MR imaging of SIRT1 expression−activity in the rat brain. The sites of increased 2-[^{18}F]BzAHA-derived-radioactivity accumulation in the rat brain (i.e., the hippo-campus, nucleus accumbens, hypothalamus, and locus coeruleus) exhibited higher levels of SIRT1 expression− activity, as demonstrated by comparative autoradiographic and immunofluorescence-microscopic (IMF) analyses of rat-brain-tissue sections. Treatment of rats with EX-527, a SIRT1-selective inhibitor, resulted in the inhibition of SIRT1 activity, as manifested by a 20−22% reduction of 2-[^{18}F]BzAHA accumulation in the nucleus accumbens, hippocampal CA3, and amygdala, as compared with baseline. Taken together, the current study demonstrated the feasibility of PET−CT−MR imaging with 2-[^{18}F]BzAHA for the noninvasive and quantitative in vivo visualization of the spatial distribution of SIRT1 expression−activity in various structures of the brain as well as for monitoring the pharmacodynamics of SIRT1 inhibitors.

RESULTS

Chemistry.

A focused library of compounds was developed for the in vitro assessment of SIRT1 catalytic activity using a carbazol-lysine-aminomethylcoumarin backbone (Cbz-Lys-AMC) derivatized at the lysine ε-amine with various benzoyland phenylacetyl-containing substituents (Figure 1 and Table S1). Compounds 1−10 were synthesized using variations of existing methodologies for the synthesis of peptidomimetics in yields between 50 and 80% with chemical purities >95%, as assessed by TLC and ^{1}H, ^{13}C, and ^{19}F NMR, and the identities of the compounds were verified by HRMS (Supporting Information). 2-Nitrophenylaminohexanoicanilide (13) was synthesized by coupling 2-nitrobenzoyl acetyl chloride with phenylhexamide in a 70% yield with >95% chemical purity and used for

subsequent radiofluorination to produce 2-[^{18}F]BzAHA (14) with high radiochemical purity >99% (Figure 1).

Enzyme-Substrate-Affinity Studies.

Enzymatic-substrate-affinity studies with a panel of recombinant SIRT1−7 enzymes demonstrated that Cbz-Lys(R)-AMC derivatized with benzoyl- or phenylacetyl-moiety-containing leaving groups (R) were effectively cleaved by SIRT1 with K_{cat} values of (0.41 ± 0.014) × 10^{-3} and (0.37 ± 0.02) × 10^{-3} s^{-1}, respectively, whereas other SIRT enzymes cleaved these moieties significantly less effectively (Figure 2 and Tables S1 and S2). As compared with nonsubstituted phenyl-based leaving groups, fluorine substitutions in the 2- and 4-positions of the benzoyl moiety resulted in about 2-fold-increased K_{cat} values for SIRT1, whereas fluorine substitution in the 3-position of benzoyl did not significantly affect the K_{cat} for SIRT1, and the 4-ethyl substitution increased the K_{cat} for SIRT1 but only minimally. Unexpectedly, the 4-iodo substitution of the benzoyl moiety resulted in a significant (40-fold) decrease in the K_{cat} for SIRT1. As compared with nonsubstituted-phenylacetyl-moiety-containing leaving groups, both 4-fluoro and 4-iodo substitutions resulted in about a 3-fold decreases in K_{cat} values for SIRT1, whereas the 2-fluoro substation of the phenylacetyl moiety resulted in a 7-fold decrease of K_{cat} for SIRT1. The 2-, 3-, and 4-fluoro-substituted benzoyl moieties were cleaved most efficiently by SIRT1, with K_{cat}/K_m values of 26.02 ± 7.07, 63.39 ± 4.32, and 16.08 ± 1.32 M^{-1} s^{-1}, respectively (Figure 2 and Table S2). The 2-fluorobenzoyl leaving group was cleaved 5-fold more effectively by SIRT1 than by any other HDAC enzyme (Figure 2B). The Cbz-Lys(2FBz)-AMC was effective as a fluorogenic substrate for a SIRT1-enzyme-activity assay in vitro (Figure 2C) and for the assessment of EX-527 inhibitory activity, yielding an IC_{50} of 12.60 μM for EX-527 (Figure 2D). Therefore, the 2-fluorobenzoyl leaving group was selected for the development of 2-[^{18}F]fluorobenzoyl-aminohexanoic anilide (2-[^{18}F]BzAHA) for the in vivo PET-imaging studies.

NMR Spectroscopy of SIRT1−2F-BzAHA-Reaction Product.

An in vitro assay of recombinant SIRT1 with 2FBzAHA monitored with ^{19}F-NMR resulted in two peaks: one at −114 ppm, corresponding to the parent compound, and one at −231 ± 3 ppm, corresponding to a reaction intermediate or product (Figures S1 and S2).

PET−CT−MR Imaging with 2-[^{18}F]BzAHA.

Dynamic PET−CT−MR imaging of rat brain with 2-[^{18}F]BzAHA demonstrated efficient crossing of the blood−brain barrier (BBB) with rapid equilibration between the blood and brain compartments within the first 2 min after iv injection (Figure S3). Significant transient accumulation of 2-[^{18}F]BzAHA-derived radioactivity was observed in the nucleus accumbens, hypothalamus, hippocampus, locus coeruleus, lateral septal nucleus, caudate putamen, and amygdala (Figures 3, 4, and S4). In contrast, the mesencephalic structures, brainstem, and cerebellum showed only minimal accumulation of 2-[^{18}F]BzAHA-derived radioactivity. The highest PET-signal contrast between different brain structures was observed at 10−20 min after the iv administration of 2-[^{18}F]BzAHA (Figures 3 and S3). Patlak graphical analysis of time−activity data in the brain using the brainstem as a reference tissue demonstrated two phases of 2-[^{18}F]BzAHA-derived-radioactivity accumulation with

different unidirectional accumulation rate constants (K_i):(a) larger K_i values 0−15 min postinjection and (b) smaller K_i values 15−60 min postinjection (Figure S5). This was consistent with the time course of the metabolic degradation of 2-[^{18}F]BzAHA (Figure S6). Logan-plot analysis also demonstrated increased accumulation in regions of the brain as compared with in the brainstem (the reference tissue), as evidenced by a slope >1 (Figure S7). Treatment of rats with the SIRT1-selective inhibitor, EX-527 (5 mg/kg ip), 30 min prior to the administration of 2-[^{18}F]BzAHA resulted in a statistically significant reduction (20−22%) of 2-[^{18}F]BzAHA-derived-radioactivity accumulation in brain regions exhibiting higher levels of SIRT1 as compared with the baseline (pretreatment) levels in the same animals ($P < 0.05$, paired Student's *t* test; Figure 5).

Radiolabeled-Metabolite Analyses.

The analyses of the time−activity profiles of 2-[^{18}F]BzAHA-derived radiolabeled metabolites in blood plasma demonstrated the rapid degradation of 2-[^{18}F]BzAHA with a monoexponential half-life of 3.8 min, resulting in a complete loss of the parent compound from plasma by 15 min after iv injection. The exact nature of the radiolabeled metabolites has not been determined. Free [^{18}F]fluoride was not detectable, consistent with the absence of radioactivity accumulation in the bones (Figure S6).

Comparative Autoradiography and Immunofluorescence-Microscopy Analyses.

Comparative analysis of PET−CT−MR images of 2-[^{18}F]BzAHA with autoradiograms of the corresponding brain sections, obtained at 20 min after iv administration of 2-[^{18}F]BzAHA (Figure S14), with the corresponding fluorescence-microscopy images of SIRT1 expression in adjacent brain-tissue sections demonstrated the colocalization of 2-[^{18}F]BzAHA-derived radioactivity with brain structures expressing high levels of SIRT1, such as the hippocampus, hypothalamus, lateral septal nucleus (LS), and nucleus accumbens (Acb, Figures 3 and S8−S14). SIRT1 expression was highest in the hippocampal CA2 and CA3 neurons (Figures 3, S8, and S9), the dentate gyrus (DG) hilus neurons, and the progenitor cells of the DG (Figure S10), whereas lower levels of SIRT1 expression were observed in the neurons of hippocampal CA1, the granular-layer neurons of the dentate gyrus, the cerebral cortex, and Acb (Figures 3 and S8−S12). Additionally, high levels of SIRT1 expression were observed in the neurons hypothalamic region adjacent to the third ventricle (Figure 4). The subcellular localization of SIRT1 in CA2 and CA3 neurons was both nuclear and perinuclear, which predominantly colocalized with (phospho-S47)SIRT1 immunofluorescence (Figure S8). Strong cytoplasmic staining for SIRT1 but not for (phospho-S47)SIRT1 was observed in the axons of several neurons in the stratum pyramidale of hippocampal CA2, traveling deeper into the stratum radiatum, as well as axons traveling into the stratum oriens (Figure S9). In DG, SIRT1 expression was observed in the perikarya of the neuronal progenitors in the subgranular zone (SGZ) and in the hilus (i.e., in pyramidal neurons, interneurons, and mossy fiber neurons; Figure S10). In the cerebral cortex, SIRT1 was predominantly expressed in large pyramidal neurons (Figure S12), whereas the subcellular distribution of SIRT1 in Acb was more uniform (Figure S11). It is noteworthy that strong SIRT1 and (phospho-S47)SIRT1 expression was observed in pericytes associated with large and medium-sized blood vessels (Figure S13).

DISCUSSION

Over the past decade, several molecular PET-imaging agents have been developed for in vivo quantitative visualization of enzyme expression and activity for different HDAC classes and isoforms, such as those for HDAC class IIa enzymes (i.e., [^{18}F]-FAHA[21] and [^{18}F]-TFAHA[19]) and those for HDAC1 enzymes (i.e., ^{11}C-Martinostat[22] and ^{18}F-MGS3[23]). Moreover, ^{11}C-Martinostat has been already translated into the clinic for mapping HDAC1 distribution in the human brain in vivo.[24] PET−CT−MR imaging with these novel imaging agents enabled the monitoring of the pharmacokinetics (PK) and BBB penetrance of nonradiolabeled drug analogues, dose−occupancy studies of HDAC class I enzymes,[25] and the dose-dependent inhibition of HDAC class IIa[18,19] enzyme activity in the brain. However, despite the biological importance of HDAC class III enzymes, especially SIRT1, PET imaging of SIRT1 expression−activity has not yet been reported.

For the development of a novel substrate-type radiotracer for quantitative molecular imaging of SIRT1 expression−activity, we studied a focused library of substrates using the Cbz-Lys-AMC backbone and various benzoyl and phenylacetyl leaving groups. This backbone has been widely used for the analysis of SIRT activity[26] and was especially useful for preliminary screening of novel potential inhibitors and activators of SIRT1, because the presence of an AMC moiety enabled high-throughput screening using fluorescence-based quantitative methods.[27] Consistent with our current results, others have also reported that a bulky lipophilic moiety (i.e., Cbz or Boc) in the cap group of the AMC-Lys(Ac) backbone aids in SIRT1 catalytic activity.[28] Furthermore, the catalytic activity and substrate selectivity of SIRTs depends not only on the backbone and cap groups but also on the leaving group.[9b] In addition to cleaving an acetyl moiety from the ε-amino terminus of lysine, different SIRT isoforms are capable of cleaving larger groups, such as malonyl (SIRT5), succinyl (SIRT5), glutaryl (SIRT5), crotonyl (SIRT3), lipoyl (SIRT4), myristoyl (SIRT2 and −6), and palmitoyl groups (SIRT4).[20,29]

Most importantly, SIRT1 can cleave ε-amino phenylacetyllysine with 56% of the natural deacetylation efficiency (Figure S15).[20]

Current SAR studies demonstrated that the catalytic efficiency of SIRT1 is greatest with a benzoyl, as opposed to a phenylacetyl, leaving group. The highest degree of SIRT1 catalytic efficiency was observed for 2-fluorobenzoyl (**2**) and 3-fluorobenzoyl (**3**) groups with K_{cat}/K_m = 26.02 and 63.39 M^{-1} s^{-1}, respectively (Figure 2 and Table S2), which was similar to K_{cat}/K_m = 65.29 M^{-1} s^{-1} of the SIRT1-mediated deacetylation of p53-derived oligopeptide Arg-His-Lys-Lys(Ac)-AMC (BPS1). Interestingly, iodine substitutions in the *para* positions of the benzoyl and phenylacetyl moieties were more deleterious to the catalytic efficiency of SIRT1 than fluorine substitutions. This is probably due to a larger van der Waals radius of the iodine atom causing steric hindrance. These SAR results for the SIRT1 catalytic cleavage of ε-amino-derivatized, halogen-substituted benzoyl- and phenylacetyl-lysine analogues are being reported herein for the first time.

Although, the 3-fluorobenzoyl leaving group (**3**) was cleaved ~60% more efficiently by SIRT1 than the 2-fluorobenzoyl leaving group (**2**), compound **2** was chosen as the lead

substrate for further development as an imaging agent because of the increased difficulty of radiolabeling **3**. Interestingly, compound **4**, containing the 4-fluorobenzoyl leaving group, was cleaved with the greatest effectiveness (the highest K_{cat})

but with a much larger K_m, thereby decreasing its catalytic efficiency, K_{cat}/K_m, to lower than that of 2 (Figure 2 and Tables S1 and S2). Novel methods for the synthesis of 4-fluorobenzoyl groups have been developed using iodonium salts[30] and copper[31] catalysts, which may be useful in the development of 3-fluorobenzoyl; however, these large salt-based or ethynyl leaving groups may be less effective for the meta position because of the increased potential for steric hindrance. In a separate study, we attempted the radiosynthesis of the 3-fluorobenzoyl group using a pinacol-derived boronic ester precursor, but the radiolabeling yield was unacceptably low (results not reported here). To facilitate clinical translation and routine production using an automated one-step radio-synthesis method, we decided to proceed with the 2-fluorobenzoyl leaving group for further studies. Furthermore, **2** demonstrated the highest selectivity as a substrate for SIRT1 when studied in a panel of recombinant SIRT1−7 and HDAC1−11 isoforms. Additionally, the SIRT1-mediated enzymatic cleavage of **2** was effectively inhibited by EX-527 (Selisistat) with an IC_{50} value of 12.6 ± 2.1 μM (Figure 2), which was 1200-fold higher than the IC_{50} of 0.0103 ± 0.0025 μM for the fluorogenic, acetylated oligopeptide substrate BPS1. Others have previously reported IC_{50} values of EX-527 for BPS1 within the same range (0.098 μM).[11a] These results suggest that 2 may also act as a competitive substrate inhibitor of SIRT1.

To create a pharmacologically optimized substrate radio-tracer, we substituted a smaller aminohexanoicanilide (AHA) for the larger Cbz-Lys-AMC backbone in compound **2**, resulting in 2-fluorobenzoyl-acetamidohexanoicanilide (2-FBzAHA). Previous studies (unpublished) have demonstrated that the Cbz-Lys-AMC backbone is unable to effectively cross the BBB because of the large size and polarity of this moiety; therefore, we have substituted a smaller lysine-mimetic, AHA, previously used for HDAC tracers.[18,19] Existing methods[32] were adapted for radiofluorination on the 2-position of the benzoyl ring for the synthesis of 2-[^{18}F]BzAHA. Initially, we developed both the 2-nitrophenylaminohexanoicanilide (2-NO_2BzAHA) and 2-trimethylamonium salt phenylaminohexanoicanilide precursors; however, after testing the radio-fluorination conditions, only 2-NO_2BzAHA provided a high yield of 2-[^{18}F]BzAHA. This is consistent with previous reports on radiolabeling using a nitro leaving group for the radiofluorination of benzoyl rings in the ortho position.[33]

The enzymatic cleavage of 2F-BzAHA by SIRT1 was validated using an in vitro SIRT1 enzyme assay and 19FNMR spectroscopy for the readout. SIRT1-mediated catalysis of 2-FPhAHA was confirmed by the presence of two peaks in the ^{19}F-NMR spectrum of the reaction products: one peak at −114 ppm (Figures S1 and S2) corresponded to the parent compound (2F-BzAHA), and a second, broader peak with a maximum at −231 ppm (Figure S2) corresponded to the reaction product (or an intermediate). Although it is difficult to fully characterize this peak, it was presumed an intermediate because it did not match the peaks of potential cleavage products, such as that of 2F-benzoic acid (−113.00 ppm), 2F-benzaldehyde (−121.32 ppm), or 2F-benzamide (−113.58 ppm, Figure S1A−D).

The established mechanism for the SIRT1-mediated catalytic cleavage of acetylated lysine is by a mixed SN1− SN2 reaction resulting in the simultaneous cleavage of nicotinamide from NAD^+ and the formation of an oxocarbenium intermediate of acetyl-lysine and the 1′ and 2′ carbons of the ribose. Subsequent nucleophilic attack by a water molecule of the tetrahedral carbon of the dioxo ring results in cleavage of the acetyl moiety from the ε-amino terminus of lysine and the formation of a 2′-O-Ac-ADPR product.[34] We hypothesized that the mechanism of substrate cleavage by SIRT enzymes should allow for the 2-[^{18}F]benzoyl group to be transferred to an adenine dinucleotide (ADN, Figure S15) and be at least transiently entrapped in the cell, similar to the [^{18}F]FDG-6-phosphate and [^{18}F]FLT-5-phosphate products of [^{18}F]FDG and [^{18}F]FLT, respectively. Also, it is conceivable that the transient nature of 2-[^{18}F]BzAHA-derived-radioactivity retention in the cells is due to the cleavage or removal of the 2-[^{18}F]benzoyl group from the ADN, similar to the previously reported cleavage of acetyl moieties from an ADN groups by esterases such as ARH3.[34,35]

Because 2-[^{18}F]BzAHA (cLogP = 4.83) is extremely lipophilic, it freely passes through the BBB, as evidenced by high levels of 2-[^{18}F]BzAHA in the brain immediately following iv injection (Figure S3). However, as previously noted, following the cleavage of 2-[^{18}F]BzAHA by SIRT1, the radiolabeled leaving group is only transiently entrapped in the cells following ester linkage to ADP-ribose. This allows for differential washout of 2-[^{18}F]BzAHA-derived radioactivity from regions of the brain with low SIRT1 expression −activity versus the transient retention of 2-[^{18}F]BzAHA-derived radioactivity in areas with high SIRT1 expression−activity (Figures 3, 4, and S3).

Analyses of radioactive metabolites in plasma after iv administration of 2-[^{18}F]BzAHA demonstrated the loss of intact parent compound after 15 min of circulation in blood (Figure S6), which explains the results of the Patlak graphical analysis,[36] which demonstrated a significant change in the unidirectional influx rate constant (K_i) from 15 min after iv administration of 2-[^{18}F]BzAHA. This is consistent with a loss of the effective input function from the intact (unmetabolized) radiotracer beyond this time point. The Patlak-plot-derived unidirectional influx rate constants (K_i) for regions of the brain with high SIRT1 expression−activity were determined using the brainstem as the reference tissue[37] (Figure S5), because brainstem nuclei have similar magnitudes of perfusion as thalamic nuclei but relatively lower levels of apparent SIRT1 expression−activity (except for the locus coeruleus). Although, radioactive metabolites of 2-[^{18}F]BzAHA dominate in blood after 20 min (Figure S6) they do not contribute significantly to the accumulation of 2-[^{18}F]BzAHA-derived radioactivity in specific brain regions. This was demonstrated by dynamic PET-imaging studies using potential radiolabeled metabolites: 2-[^{18}F]benzaldehyde and 2-[^{18}F]ethyl benzoate metabolized in vivo to 2-[^{18}F]benzoic acid (Figure S16A). These radiotracers demonstrated significantly different patterns of radioactivity distribution in the brain, as compared with that of 2- [^{18}F]BzAHA (Figure S16B). Most notably, increased 2-[^{18}F]benzaldehyde-derived-radioactivity accumulation was observed in the brainstem, which was contrary to the absence of 2-[^{18}F]BzAHA-derived-radioactivity accumulation in this region (Figure S16B).

Dynamic PET−CT−MR images acquired in normal rats using 2-[^{18}F]BzAHA demonstrated significant retention of 2-[^{18}F]BzAHA-derived radioactivity in areas of the brain with relatively higher SIRT1 expression (i.e., hypothalamus, hippocampus, septal nucleus, nucleus accumbens, and locus coeruleus). These in vivo imaging results have been validated by comparative in situ autoradiography and immunofluorescence-microscopy (IFM) studies (Figures 3, 4, and S7−S13). Autoradiography provided high-resolution (~100 × 100 μm) images of 2-[^{18}F]BzAHA distribution and localization of increased radioactivity accumulation in the brain, whereas IFM provided confirmation of cellular and subcellular localization of total SIRT1 and phospho-SIRT1 expression in the corresponding brain regions. The results of these comparative in vivo−in situ validation studies confirmed that noninvasive PET imaging with 2-[^{18}F]BzAHA accurately reflects the sites of increased SIRT1 expression−activity in the rat brain and are in agreement with previously published reports on the distribution and roles of SIRT1 expression in the rat brain using ISH and IF,[38] described in greater detail below.

High levels of 2-[^{18}F]BzAHA-derived radioactivity and SIRT1 immunofluorescence observed in the hippocampus (Figures 3, S8−S10, and S14) are consistent with previous studies using ISH,[38a] IHC,[38b] and IF.[39] SIRT1 is involved in mechanisms of learning and memory (both short- and long-term); it modulates synaptic plasticity through transcriptional regulation of a brain-derived neurotrophic factor via MeCP2 deacetylation.[40] Accordingly, animals deficient in SIRT1 demonstrate deficits in memory formation and related cognitive functions.[39] Our IFM analyses demonstrated increased levels of SIRT1 expression particularly in CA2− CA3 neurons, with lower levels of expression in CA1 neurons (Figures S8−S10). Within the neurons, SIRT1 exhibited mixed nuclear and perinuclear localization, although the perinuclear localization was more pronounced. Furthermore, increased levels of SIRT1 expression were observed in many pyramidal axons traveling deeper into the hippocampal layers, as well as axons of neurons of the inner and outer molecular layers traveling toward the alveus. These Schaffer collateral pathways demonstrate high levels of SIRT1 expression, consistent with the role of SIRT1 as a potent mediator of long-term potentiation.[39] Evidence for the role of SIRT1 in hippocampal progenitor cells within the dentate gyrus has been previously reported in mice[41] and is consistent with the results of our IMF studies (Figure S10). Also, SIRT1-mediated regulation plays an important role in the development of aging-associated neurocognitive decline, as demonstrated by the decreased degeneration of pyramidal neurons in Ammon's horn in aging rats as a result of treatment with resveratrol, a naturally occurring activator of SIRT1.[42] The age-related differences in SIRT1 activity can be linked to changes in p53 acetylation in the CA2−3 regions.[43] Decreases in SIRT1 activity within the hippocampus have also been linked to chronic stress, depressive behaviors,[44] and Alzheimer's Disease progression, as decreased SIRT1 expression within the entorhinal cortex and hippocampus correlates to higher tau loads and amyloid-β deposits.[45] Changes in SIRT1 expression may be quite dynamic in many of these pathological conditions, such as in the progressive decline in cognitive-memory performance with increasing body-mass index in animals with dietary-induced obesity; however, treatment with a SIRT1-targeted activator, resveratrol, ameliorates much of the hippocampal neuro-degeneration.[46] Alternatively, increased SIRT1-expression levels have been noted in other neurodegenerative diseases, such as Huntington's disease, which has led to exploratory

clinical trials with SIRT1 selective inhibitors, such as Selisistat (EX-527)[47].[15e] Because of the pleiotropic role of SIRT1 in neurodegeneration, there is an ongoing debate in the literature regarding the effectiveness of SIRT1 activators versus inhibitors for the treatment of neurodegeneration.[48] Therefore, PET imaging of SIRT1 activity with 2-[^{18}F]BzAHA should facilitate the development and clinical translation of novel potent SIRT1 activators and inhibitors for neuroprotection, prevention, and therapy of various neurodegenerative diseases and age-related neurocognitive decline.

Another important finding in the current study using PET− CT−MRI with 2-[^{18}F]BzAHA was the high level of SIRT1 expression−activity in the nucleus accumbens (Figures 3 and S11), which is consistent with previous reports of increased levels of SIRT1 expression demonstrated by ISH[38a] and IHC.[38b] Within the nucleus accumbens (Acb), SIRT1 was shown to deacetylate FOXO3a and to increase the expression of several target genes that enhance cocaine-addiction behaviors.[49] Furthermore, chronic cocaine usage has been demonstrated to increase SIRT1 activity within the Acb and SIRT1-mRNA production through an increase in the acetylation of the gene promoter for SIRT1 transcription.[50] Therefore, PET imaging of SIRT1 expression−activity with 2-[^{18}F]BzAHA may advance our understanding of mechanisms of addiction and aid in the development of new therapies for addictive disorders.

Increased levels of 2-[^{18}F]BzAHA-derived radioactivity and SIRT1 immunofluorescence observed in the hypothalamus (Figure 4) are also consistent with previous reports using ISH,[38a] IHC,[38b,51] and IF.[52] SIRT1 plays a key role in many important functions, such as the central regulation of metabolism, body temperature, feeding, and circadian rhythm. In the neurons of the arcuate nucleus, SIRT1 is expressed in pro-opiomelanocortin (POMC) and agouti-related peptide (AgRP)-expressing neurons and regulates energy expenditure.[40] SIRT1 localization to the POMC neurons in the arcuate nucleus surrounding the third ventricle was observed using IMF, confirming the involvement of SIRT1 in the central regulation of metabolism.[52] Additionally, SIRT1 regulates SF1 neurons in the ventromedial hypothalamus to regulate energy homeostasis.[53] SIRT1 is crucial to the hypothalamic response to glucose, insulin, and leptin[54] and serves as potential target for the treatment of diabetes and obesity. Several studies have demonstrated that SIRT1 overexpression can rescue obesity-induced insulin resistance through increased levels of FOXO1 deacetylation in POMC neurons.[55] Clinical trials have been conducted to test the ability of SIRT1-activators (i.e., resveratrol, SRT2104, and nicotinamide riboside) as therapeutic agents for type-2 diabetes and obesity (i.e., NCT01677611 and NCT01150955).[56] Thus, imaging of SIRT1 expression−activity using PET−CT−MRI with 2-[^{18}F]BzAHA may advance the understanding of the mechanisms of the hypothalamic regulation of metabolism and normal and disease conditions and facilitate the development and clinical evaluation of novel SIRT1-targeted therapies for metabolic diseases.

Furthermore, our observation of high levels of 2-[^{18}F]BzAHA-derived radioactivity in the locus coeruleus (LC, Figure 4) is consistent with previous reports of increased levels of SIRT1 expression as determined by IHC and IF.[57] Because of the extremely small size of the LC in the rat brain (~1 mm), the partial volume effect is substantial because of the relatively low in-plane resolution of microPET R4 (~2 mm), which is the main reason for the low

intensity and asymmetry of 2-[^{18}F]BzAHA-derived signals on PET−CT−MR images of LC (Figure 4). It has been demonstrated that SIRT1 plays a significant regulatory role within neurons of the LC, particularly in the sleep−wake cycle.[40,57] Additionally, increased acetylation of histone core proteins H3 and H4 within the dorsal raphe nucleus and LC were noted in less resilient rats exposed to chronic stress as compared with in rats with increased resiliency. Hyperacetylation of H3 and H4 has been linked to decreased levels of SIRT1 expression.[58] Because of the extensive involvement of the LC within many brain-circuitry functions, including metabolism, stress, wakefulness, addiction, and neurodegeneration, the ability to noninvasively image and monitor SIRT1 expression−activity within this key structure of the brain may aid in the development of novel treatments of various neurological and metabolic diseases.

The absence of 2-[^{18}F]BzAHA-derived-radioactivity accumulation in other brainstem structures, as seen in PET imaging, autoradiography, and IMF, is consistent with reports using ISH.[38a] Low levels of SIRT1 expression in the brainstem provide the opportunity for accurate quantification of 2-[^{18}F]BzAHA-derived-radioactivity accumulation in other regions of the brain through the use of the reference-tissue-based Patlak graphical-analysis method[37] between 0 and 20 min after radiotracer administration, with the parent 2-[^{18}F]BzAHA present in the blood (Figure S5). Also, because of the transient (reversible) nature of the entrapment of 2-[^{18}F]BzAHA-derived radioactivity, the apparent volumes of the distribution of 2-[^{18}F]BzAHA, reflecting the SIRT1-expression−activity product, can be calculated using Logan graphical analysis[59] with the brainstem as a reference tissue (Figure S7).

Current studies also underscore the important role of SIRT1 in brain vasculature. Throughout the brain, there is strong expression of both SIRT1 and phospho-SIRT1 in pericytes (Figure S13), which supports the role of SIRT1 in the eNOS-mediated regulation of cerebral blood flow.[60] Pretreatment of rats with a natural SIRT1-activator, resveratrol, prior to an ischemic event confers neuroprotection to the hippocampal pyramidal neurons.[61] Additionally, in disease conditions, SIRT1 is a direct modifier of HIF-1α, thereby stabilizing the protein under hypoxia to promote the transcription of many inducible gene targets, such as VEGF and MMP1.[62] Therefore, PET imaging SIRT1 expression−activity in the brain may advance the understanding of SIRT1 roles in vascular maintenance and remodeling following ischemia−reperfusion events (i.e., atherosclerotic and other angiopathies, brain infarctions, or trauma).

Also, the current study demonstrated the feasibility of 2-[^{18}F]BzAHA PET−CT−MRI for noninvasive, in vivo monitoring of the pharmacodynamics of the SIRT1-specific inhibitor EX-527 at the target level (inhibition of SIRT1 enzyme activity). A statistically significant decrease in 2-[^{18}F]BzAHA-derived-radioactivity accumulation in the brain was observed after administration of EX-527, as compared with pretreatment levels, especially in the brain structures exhibiting higher levels of SIRT1 expression−activity at baseline (i.e., the hippocampus, nucleus accumbens, and amygdala; Figure 5). The dose of EX-527 used in this study was chosen to be similar to doses used in previously published reports;[11a] however, this dose demonstrated only a 20% inhibition of 2-[^{18}F]BzAHA-derived-radioactivity accumulation. This observation suggests that higher doses of EX-527 may be

required to achieve more inhibition of SIRT1 in these brain structures. Furthermore, the BBB penetrability of EX-527 has not yet been well established, and this may be a limiting factor to SIRT1 inhibition in the CNS. Using PET−MRI with 2-[^{18}F]BzAHA, it should be possible to determine the IC_{50} doses of EX-527 and other SIRT1-specific inhibitors or activators in different structures of the brain by imaging the same subject after the administration of increasing doses of inhibitor, as reported by us previously for SAHA.[21a]

CONCLUSIONS

In summary, we have demonstrated that PET−CT−MRI imaging with the newly developed first-generation SIRT1-selective radiotracer, 2-[^{18}F]BzAHA, can be used for noninvasive, repetitive, and quantitative visualization of SIRT1 expression−activity in the brain. Molecular imaging with PET−CT−MRI using SIRT1-specific substrate-type radio-tracers should improve the understanding of the many roles that SIRT1 plays in normal brain physiology and in various brain diseases and pathological states and will facilitate the development and clinical translation of novel SIRT1-specific activators and inhibitors.

EXPERIMENTAL SECTION

All solvents were purchased from Sigma-Aldrich Chemicals (Milwaukee, WI) and used without further purification. Boc-Lys(Ac)-AMC and Cbz-Lys-OH were purchased from Bachem (Bubendorf, Switzerland) and used without further purification. 6-Amino-1-hexanoicanilide was synthesized using a previously published procedure.[63] Thin-layer chromatography (TLC) was performed on precoated Dynamic Absorbance F-254 silica-gel aluminum-backed plates (Norcross, GA); flash chromatography was performed using silica gel (pore size 60 Å, 230−400 mesh particle size; Sigma-Aldrich, Milwaukee, WI). ^{1}H, ^{13}C, and ^{19}F NMR spectroscopy was performed using a Mercury 400 MHz, Varian 500 MHz, or Agilent 600 MHz spectrometer. High-resolution mass spectra (HRMS) were obtained using a Waters LCT Premier/XE spectrometer (Milford, MA) with an electrospray-ionization (ESI) technique. The analytical high-performance-liquid-chromatography (HPLC) system included an Ascentis RP-Amide 4.4 × 150 mm column (Supelco, Bellefonte, PA) connected to a 1100 series pump, a UV detector (Agilent Technologies, Stuttgart, Germany) operated at 254 nm, and an FC3200 radioactivity detector (Eckert and Ziegler Radiopharma, Inc., Berlin, Germany). The semipreparative-HPLC system included an Alltima 250 × 10 mm C18 column (Fisher Scientific, Waltham, MA) connected to a P4.1S pump, an Azura 2.1S UV detector (Knauer, Berlin, Germany) operated at 254 nm, and an FC-3500 radioactivity detector (Eckert and Ziegler Radiopharma, Inc., Berlin, Germany). In general, TLC and HRMS were used to determine the purities of synthesized nonradiolabeled compounds; radio-TLC and combined UV−radio-HPLC were used to determine the purities of radiolabeled compounds. The threshold of acceptable purity was set at ≥95%.

Chemical Synthesis.

Compounds **1−10** were prepared following previously published methods[29c,64] with minor modifications, as shown in Figure 1. Compounds **1−10** were synthesized following published methods[29c] from commercially available Cbz-lysine with a formation of the corresponding acetyl chloride, which, upon reaction with AMC (**2**) in the presence of $POCl_3$

and pyridine, provided the desired product in moderate to good yields. To synthesize compound 4, Cbz-Lys (1 equiv) was dissolved in a mixture of THF (5 mL) and water (5 mL); then, sodium bicarbonate (2 equiv) and a solution of Boc_2O (2.3 equiv) in THF (5 mL) were added. After the solution was stirred at room temperature overnight, the THF was removed under reduced pressure, and the resulting aqueous solution was neutralized with 2 N HCl. The mixture was extracted with ethyl acetate, and the combined organic layers were washed with brine. The organic layer was dried with sodium sulfate and concentrated to a clear oil, which was used for further reactions, without any purification, with 2 in the presence of NMM/isobutyl chloroformate (Figure 2).

Benzyl (6-Benzamido-1-((4-methyl-2-oxo-2H-chromen-7-yl)-amino)-1-oxohexan-2-yl)carbamate (1).—Compound **1** was synthesized by the method described above using benzoyl chloride (Sigma, Milwaukee, WI) as the reacting R group. The resulting product was run on a chromatograph with 5% methanol in dichloromethane. ^{1}H, ^{13}C, and ^{19}F NMR were used to determine the molecular characterization of this compound, and TLC and HRMS determined >95% purity. Yield: 63%, ^{1}H NMR ($CDCl_3$, 600 MHz): δ 9.38 (s, 1H), 7.76 (d, 2H, J = 7.8 Hz), 7.68 (s, 1H), 7.602−7.46 (m, 3H), 7.39−7.34 (m, 7H), 6.18 (s, 1H), 5.95 (d, 1H, J = 7.2 Hz), 5.11 (m, 2H), 4.41 (s, 1H), 3.49 (m, 1H), 2.40 (s, 3H), 2.07−2.05 (m, 1H), 1.88−1.80 (m, 1H), 1.70−1.64 (m, 2H), 1.56−1.50 (m, 2H). ^{13}C NMR ($CDCl_3$, 600 MHz): δ 171.00, 168.24, 161.26, 156.92, 154.07, 152.46, 141.47, 136.08, 134.25, 134.23, 131.61, 128.61 (2C), 128.25, 128.02, 126.92 (2C), 125.10, 116.04, 115.84, 11.31, 107.30, 67.28, 55.41, 38.73, 38.60, 31.24, 29.71, 28.75, 22.26, 18.56. MS (EI): *m/z* 542.6 [M + H]. High-resolution MS: calculated for $C_{31}H_{31}N_3O_6$ $[M + Na]^+$ 564.2111, found 564.2105.

Benzyl (6-(2-Fluorobenzamido)-1-((4-methyl-2-oxo-2H-chromen-7-yl)amino)-1-oxohexan-2-yl)carbamate (2).—Compound **2** was synthesized by the method described above using 2-fluorobenzoyl chloride (Sigma, Milwaukee, WI) as the reacting R group. The resulting product was run on a chromatograph with 3% methanol/dichloromethane and purified by combiflash with 5% methanol/dichloromethane. ^{1}H, ^{13}C, and ^{19}F NMR were used to determine the molecular characterization of this compound, and TLC and HRMS determined >95% purity. Yield: 69%, ^{1}H NMR (DMSO-d_6, 600 MHz): δ 10.51 (s, 1H), 8.29 (s, 1H), 7.77 (brs, 1H), 7.71 (d, 1H, J = 8.4 Hz), 7.65 (d, 1H, J = 7.8 Hz), 7.54 (t, 1H, J = 7.2 Hz), 7.50−7.47 (m, 2H), 7.38−7.31 (m, 4H), 7.24−7.17 (m, 2H), 6.27 (s, 1H), 5.03 (s, 2H), 4.16 (m, 1H), 3.24 (q, 2H, J = 6.6 Hz), 2.40 (s, 3H), 1.72−1.66 (m, 2H), 1.56−1.38 (m, 4H). ^{13}C NMR (DMSO-d_6, 600 MHz): δ 172.49, 164.15, 160.59, 160.28, 158.63, 156.65, 154.09, 153.68, 142.67, 137.39, 132.66, 130.42, 128.84 (2C), 128.32 (2C), 126.41, 124.85, 116.55, 116.40, 115.77, 115.56, 112.75, 106.19, 65.98, 56.05, 39.33, 31.74, 29.04, 23.39, 18.45.^{19}F (DMSO-d_6, 300 MHz): δ −114.49. MS (EI): *m/z* 560.6 [M + H]. High-resolution MS: calculated for $C_{31}H_{30}FN_3O_6$ $[M + Na]^+$ 582.2016, found 582.1989.

Benzyl (6-(3-Fluorobenzamido)-1-((4-methyl-2-oxo-2H-chromen-7-yl)amino)-1-oxohexan-2-yl)carbamate (3).—Compound **3** was synthesized by the method described above using 3-fluorobenzoyl chloride (Sigma, Milwaukee, WI) as the reacting R group. The resulting product was run on a chromatograph with 3% methanol in dichloromethane and

purified by combiflash with 5% methanol/dichloromethane. ^{1}H, ^{13}C, and ^{19}F NMR were used to determine the molecular characterization of this compound, and TLC and HRMS determined >95% purity. Yield: 66%, ^{1}H NMR ($CDCl_3$): δ 9.19 (brs, 1H), 7.67 (s, 1H), 7.55−7.49 (m, 4H), 7.46−7.351 (m, 6H), 7.20 (t, 1H, J = 7.8 Hz), 6.56 (brs, 1H), 6.22 (s, 1H), 5.85 (brs, 1H), 5.14 (m, 2H), 4.40 (s, 1H), 3.51 (m, 2H), 2.43 (s, 3H), 2.07−2.06 (m, 1H), 1.88−1.80 (m, 1H), 1.72−1.60 (m, 2H), 1.56−1.52 (m, 2H). ^{13}C NMR ($CDCl_3$): δ 170.56, 166.86, 163.54, 161.18, 154.11, 152.21, 141.10, 136.00, 130.32, 128.59 (2C), 128.31, 128.06 (2C), 125.14, 122.43, 118.66, 118.52, 116.15, 115.80, 114.41, 114.27, 113.41, 107.31, 67.36, 55.34, 38.73, 30.95, 28.61, 22.16, 18.59. ^{19}F ($CDCl_3$, 300 MHz): δ −111.60. MS (EI): *m/z* 560.6 [M + H]. High-resolution MS: calculated for $C_{31}H_{30}FN_3O_6$ $[M + Na]^+$ 582.2016, found 582.1986.

Benzyl (6-(4-Fluorobenzamido)-1-((4-methyl-2-oxo-2H-chromen-7-yl)amino)-1-oxohexan-2-yl)carbamate (4).—Compound **4** was synthesized by the method described above using 4-fluorobenzoyl chloride (Sigma, Milwaukee, WI) as the reacting R group. The resulting product was run on a chromatograph with 5% methanol in dichloromethane and purified by combiflash with 5% methanol/dichloromethane. ^{1}H, ^{13}C, and ^{19}F NMR were used to determine the molecular characterization of this compound, and TLC and HRMS determined >95% purity. Yield: 72%, ^{1}H NMR ($CDCl_3$): δ 9.38 (s, 1H), 7.78 (m, 2H), 7.66 (s, 1H), 7.51−7.45 (m, 2H), 7.39−7.33 (m, 5H), 6.99 (t, 2H, 6J), 6.65 (t, 1H, J = 6 Hz), 6.15 (s, 1H), 6.02 (d, 1H, J = 8 Hz), 5.11 (s, 2H), 4.45 (brs, 1H), 3.49−3.46 (m, 2H), 2.39 (s, 3H), 2.01−1.88 (m, 2H), 1.71−1.67 (m, 2H), 1.55−1.50 (m, 2H). ^{13}C NMR ($CDCl_3$): δ 170.91, 167.16, 165.59, 161.17, 154.1, 152.36, 141.37, 136.00, 130.38 (2C), 129.31 (2C), 129.25, 128.60 (2C), 128.32, 128.06, 125.13, 116.12, 115.80, 115.69, 115.54, 113.40, 107.30, 67.37, 55.38, 38.66, 30.93, 28.69, 22.17, 18.57. ^{19}F ($CDCl_3$, 300 MHz): δ −107.70. MS (EI): m/z 560.6 [M + H]. High-resolution MS: calculated for $C_{31}H_{30}FN_3O_6$ $[M + Na]^+$ 582.2016, found 582.1985.

Benzyl (6-(4-Ethylbenzamido)-1-((4-methyl-2-oxo-2H-chromen-7-yl)amino)-1-oxohexan-2-yl)carbamate (5).—Compound **10** was synthesized by the method described above using 4-ethylbenzoyl chloride (Sigma, Milwaukee, WI) as the reacting R group. The resulting product was run on a chromatograph with 5% methanol in dichloromethane and purified by combiflash with 5% methanol/dichloromethane. ^{1}H, ^{13}C, and ^{19}F NMR were used to determine the molecular characterization of this compound, and TLC and HRMS determined >95% purity. Yield: 77%, ^{1}H NMR ($CDCl_3$): δ 9.71 (s, 1H), 7.68 (m, 3H), 7.44−7.39 (m, 2H), 7.38−7.30 (m, 4H), 7.12 (d, 2H, J = 7.8 Hz), 6.87 (s, 1H), 6.26 (d, 1H, J = 7.8 Hz), 6.11 (s, 1H), 5.07 (s, 2H), 4.45 (brs, 1H), 3.42 (m, 2H), 2.62 (q, 2H, J = 7.2 Hz), 2.44 (s, 3H), 1.98−1.82 (m, 2H), 1.67−1.48 (m, 4H), 1.19 (t, 3H, J = 7.2 Hz). ^{13}C NMR ($CDCl_3$): δ 171.55, 168.20, 161.40, 156.88, 153.89, 152.75, 148.11, 141.63, 136.17, 131.90, 128.51 (2C), 128.13, 127.97 (2C), 127.89, 127.10 (3C), 125.05, 115.93, 115.84, 113.52, 107.21, 67.14, 55.65, 39.09, 31.78, 28.89, 28.70, 22.55, 18.51, 15.27. MS (EI): *m/z* 570.7 [M + H]. High-resolution MS: calculated for $C_{33}H_{35}N_3O_6$ $[M + Na]^+$ 592.2424, found 592.2433.

Benzyl (6-(4-Iodobenzamido)-1-((4-methyl-2-oxo-2H-chromen-7-yl)amino)-1-oxohexan-2-yl)carbamate (6).—Compound **6** was synthesized by the method described above using 4-iodobenzoyl chloride (Sigma, Milwaukee, WI) as the reacting R group. The resulting product was run on a chromatograph with 5% methanol in dichloromethane and purified by combiflash with 5% methanol/dichloromethane. ^{1}H, ^{13}C, and ^{19}F NMR were used to determine the molecular characterization of this compound, and TLC and HRMS determined >95% purity. Yield: 60%, ^{1}H NMR ($CDCl_3$): δ 9.17 (s, 1H), 7.69−7.66 (m, 3H), 7.54−7.46 (m, 4H), 7.42−7.34 (m, 5H), 6.21 (s, 1H), 5.86 (brs, 1H), 5.12 (s, 2H), 4.38 (brs, 1H), 3.55−3.44 (m, 2H), 2.43 (s, 3H), 2.10−2.06 (m, 1H), 1.89−1.84 (m, 1H), 1.71−1.68 (m, 2H), 1.57−1.50 (m, 2H). ^{13}C NMR (MeOD): δ 171.50, 166.21, 160.30, 155.42, 152.20, 135.86, 132.30 (2C), 126.97, 126.58 (2C), 126.15, 125.96, 123.76, 122.76, 120.18, 119.09, 118.70, 116.95, 114.96, 114.32, 110.82, 105.17, 96.01, 64.87, 54.25, 37.45, 29.90, 27.00, 21.10, 15.70. MS (EI): *m/z* 667.5 [M+]. High-resolution MS: calculated for $C_{31}H_{30}IN_3O_6$ $[M + Na]^+$ 690.1077, found 690.1075.

Benzyl (1-((4-Methyl-2-oxo-2H-chromen-7-yl)amino-1-oxo-6-(2-phenylacetamido)hexan-2-yl)carbamate (7).—Compound 7 was prepared following the method described above using phenyl acetyl chloride (Sigma, Milwaukee, WI) as the reacting R group. The resulting product was run on a chromatograph with 3% methanol in dichloromethane and purified by combiflash with 5% methanol/dichloromethane. ^{1}H, ^{13}C, and ^{19}F NMR were used to determine the molecular characterization of this compound, and TLC and HRMS determined >95% purity. Yield: 59%, This is a known compound,[29c] so here we report MS (EI): *m/z* 554.6 [M − H]. High-resolution MS: calculated for $C_{32}H_{33}N_3O_6$ $[M + Na]^+$ 578.2267, found 578.2269.

Benzyl (6-(2-(2-Fluorophenyl)acetamido)-1-((4-methyl-2-oxo-2H-chromen-7-yl)amino)-1-oxohexan-2-yl)carbamate (8).—Compound 8 was synthesized by the method described above using 2-fluorophenyl acetyl chloride (Sigma, Milwaukee, WI) as the reacting R group. The resulting product was run on a chromatograph with 3% methanol in dichloromethane and purified by combiflash with 5% methanol/dichloromethane. ^{1}H, ^{13}C, and ^{19}F NMR were used to determine the molecular characterization of this compound, and TLC and HRMS determined >95% purity. Yield: 57%, ^{1}H NMR (DMSO-d_6): δ 10.52 (s, 1H), 8.06 (t, 1H, J = 5.4 Hz), 7.78 (s, 1H), 7.73−7.64 (m, 2H), 7.51 (s, 1H), 7.37−7.24 (m, 7H), 7.12−7.09 (m, 2H), 6.27 (s, 1H), 5.04 (s, 2H), 4.13 (m, 1H), 3.04 (m, 2H), 2.40 (s, 3H), 1.68−1.33 (m, 6H). ^{13}C NMR (DMSO-d_6): δ 172.10, 169.51, 167.22, 160.38, 156.18, 154.00, 153.68, 142.69, 137.39, 132.19, 129.14, 129.01 (2C), 128.96, 128.85 (2C), 126.45, 124.60, 122.62, 115.79, 115.57, 115.48, 112.76, 106.19, 65.99, 55.33, 38.98, 35.74, 31.17, 28.81, 22.85, 18.45. ^{19}F (DMSO-d_6, 300 MHz): δ −117.40. MS (EI): *m/z* 572.6 [M − H]. High-resolution MS: calculated for $C_{32}H_{32}FN_3O_6$ $[M + Na]^+$ 596.2173, found 596.2180.

Benzyl (6-(2-(4-Fluorophenyl)acetamido)-1-((4-methyl-2-oxo-2H-chromen-7-yl)amino)-1-oxohexan-2-yl)carbamate (9).—Compound **9** was synthesized by the method described above using 4-fluorophenyl acetyl chloride (Sigma, Milwaukee, WI) as the reacting R group. The resulting product was run on a chromatograph with 3% methanol in dichloromethane and purified by combiflash with 5% methanol/dichloromethane. ^{1}H,

^{13}C, and ^{19}F NMR were used to determine the molecular characterization of this compound, and TLC and HRMS determined >95% purity. Yield: 60%, ^{1}H NMR (MeOD): δ 7.78 (s, 1H), 7.67 (d, 1H, J = 8.2 Hz), 7.46 (d, 1H, J = 2 Hz), 7.39−7.25 (m, 7H), 7.00−6.97 (m, 2H), 6.22 (s, 1H), 5.12−5.11 (m, 2H), 4.26 (t, 1H, J = 5.3 Hz), 3.45 (s, 2H), 3.19 (t, 2H, J = 6.6 Hz), 2.45 (s, 3H), 1.86−1.74 (m, 2H), 1.56−1.40 (m, 4H). ^{13}C NMR (MeOD): δ 172.44, 172.36, 162.70, 161.81, 161.08, 157.23, 153.91, 153.82, 141.94, 136.74, 131.58, 130.61, 130.40, 130.35, 128.09, 127.66, 127.48, 125.27, 115.82, 115.79, 114.81, 114.76, 112.22, 106.66, 66.40, 55.83, 42.37, 38.79, 31.46, 28.58, 22.82, 17.12. ^{19}F (MeOD, 300 MHz): δ −118.40. MS (EI): *m/z* 574.7 [M + H]. High-resolution MS: calculated for $C_{32}H_{32}FN_3O_6$ $[M + Na]^+$ 596.2173, found 596.2173.

Benzyl (6-(2-(4-Iodophenyl)acetamido)-1-((4-methyl-2-oxo-2H-chromen-7-yl)amino)-1-oxohexan-2-yl)carbamate (10).—Compound **10** was synthesized by the method described above using 4-iodophenyl acetyl chloride (Sigma, Milwaukee, WI) as the reacting R group. The resulting product was run on a chromatograph with 3% methanol in dichloromethane and purified by combiflash with 5% methanol/dichloromethane. ^{1}H, ^{13}C, and ^{19}F NMR were used to determine the molecular characterization of this compound, and TLC and HRMS determined >95% purity. Yield: 72%, ^{1}H NMR (MeOD): δ 8.11 (brs, 1H), 7.88 (d, 1H, J = 8.4 Hz), 7.82 (s, 1H), 7.76−7.73 (m, 2H), 7.67 (d, 1H, J = 8.4 Hz), 7.61 (d, 1H, J = 7.8 Hz), 7.54−7.48 (m, 2H), 7.40−7.31 (m, 2H), 7.09 (d, 1H, J = 7.8 Hz), 7.04 (d, 1H, J = 8.4 Hz), 6.26 (s, 1H), 5.13 (m, 2H), 4.25 (m, 1H), 3.43 (s, 2H), 3.21 (m, 2H), 2.48 (s, 3H), 1.89−1.74 (m, 2H), 1.56−1.48 (m, 4H). ^{13}C NMR (MeOD): δ 172.04, 171.92, 161.87, 154.00, 153.89, 137.31 (2C), 137.23, 135.45, 131.20, 130.80 (2C), 128.09, 127.67, 127.50, 126.50, 125.35, 115.91, 115.86, 112.26, 106.72, 91.30, 66.41, 55.80, 41.83, 38.53, 31.45, 28.53, 22.78, 17.15. MS (EI): m/z 680.4 [M − H]. High-resolution MS: calculated for $C_{32}H_{32}IN_3O_6$ $[M + Na]^+$ 704.1233, found 704.1231.

2-Fluoro-phenylhexanoicanilide, 2-FPhAHA (12).—Compound **11** (0.240g, 1.163 mmol) was dissolved in 5 mL of dichloromethane and 0.5 mL of triethylamine. The 2-fluoro benzoyl chloride (0.2 mL, 1.696 mmol) was added dropwise at 0°C. The reaction was stirred at 0°C for 30 min, then gradually warmed to RT, and stirred under argon for 3 h. The mixture was washed with ethyl acetate and a 4 N HCl solution. The organic layer was dried over magnesium sulfate and then evaporated to dryness. The resulting crude mixture was recrystallized with diethyl-ether overnight and then filtered by vacuum filtration before being dried under high vacuum. Product 12 (110 mg) was made as a white solid in 28% yield. ^{1}H, ^{13}C, and ^{19}F NMR were used to determine the molecular characterization of this compound, and TLC and HRMS determined >95% purity. ^{1}H NMR (DMSO-d_6): δ 9.87 (s, 1H), 8.31 (s, 1H) 7.54 (m, 4H), 7.25 (dt, J = 7.8 Hz, 4H), 7.01 (t, 1H), 3.24 (dd, J = 5.9 Hz, 2H), 2.31 (t, J = 7.3 Hz, 2H), 1.62 (m, 4H), 1.35 (m, 2H). ^{13}C NMR (101 MHz, $CDCl_3$): δ 171.33, 163.47, 161.73, 159.28, 138.18, 133.15 (d, J = 9.3 Hz), 131.82, 128.86, 124.75 (d, J = 3.1 Hz), 124.00, 121.21 (d, J = 11.3 Hz), 119.82, 115.98 (d, J = 24.8 Hz), 77.35, 77.03, 76.71, 39.74, 37.32, 29.17, 26.36, 25.02. ^{19}F NMR: δ −114.64. High-resolution MS: calculated $[M + Na]^+$ 329.1665, found 329.1654.

2-Nitro-N-(6-oxo-6-(phenylamino)hexyl)benzamide (13).—A solution of 2-nitrobenzoyl chloride (0.12 g, 0.62 mmol) in 0.5 mL of DCM was added dropwise to a mixture of phenylhexanamide (**11**, 0.10 g, 0.48 mmol) and diisopropylethylamine (DIPEA, 0.13 mL, 0.73 mmol) in dimethylformamide (5 mL) at 0°C; then, the solution was left to stir at room temperature for 12 h. The solvent was then evaporated under reduced pressure; the crude was dissolved in EtOAc and washed with water. The organic layer was dried over sodium sulfate. Evaporation and purification with column chromatography (eluent of EtOAc) gave the desired precursor, 13, in a 70−72% yield. ^{1}H, ^{13}C, and ^{19}F NMR were used to determine the molecular characterization of this compound, and TLC and HRMS determined >95% purity. ^{1}H NMR (600 MHz, DMSO-d_6): δ 9.87 (s, 1H), 8.66 (t, J = 5.5 Hz, 1H), 8.02 (d, J = 8.1 Hz, 1H), 7.75 (t, J = 7.5 Hz, 1H), 7.67 (t, J = 7.8 Hz, 1H), 7.60 (d, J = 8.2 Hz, 2H), 7.57 (d, J = 7.5 Hz, 1H), 7.28 (t, J = 7.8 Hz, 2H), 7.01 (t, J = 7.3 Hz, 1H), 3.22 (dd, J = 12.9, 6.6 Hz, 2H), 2.32 (t, J = 7.4 Hz, 2H), 1.67−1.59 (m, 2H), 1.58−1.50 (m, 2H), 1.42−1.33 (m, 2H). ^{13}C NMR (151 MHz, DMSO-d_6): δ 171.2, 165.3, 147.0, 139.4, 133.5, 132.8, 130.5, 129.0, 128.6, 124.0, 122.9, 119.0, 39.0, 36.4, 28.6, 26.1, 24.8. High-resolution MS: calculated $[M + Na]^+$ 356.1600, found 356.1598.

Radiosynthesis of 2-[^{18}F]-Fluorobenzoyl-aminohexanoicanilide, 2-[^{18}F]BzAHA (14).—The F-18 was obtained in a kryptofix/K[^{18}F] complex in acetonitrile/water (1 mL) from the PET/Cyclotron Facility, Wayne State University, Detroit, MI, and transferred into a crimped 2 mL V-vial for azeotropic drying. Acetonitrile (0.4 mL) was added to the mixture, which was dried under a stream of argon at 90− 100°C. A solution of 13 (~2 mg) in dry dimethyl sulfoxide (0.4 mL) was added to the dried kryptofix/K[^{18}F] and heated to 130−140°C under argon with stirring for 12 min. After cooling, the reaction mixture was passed through a 900 mg Altech silica-gel cartridge (Fisher Scientific, Waltham, MA) and eluted with 2 mL of 10% methanol in dichloromethane (DCM). The solvent was evaporated under a stream of argon to remove DCM and to reduce the volume to <0.5 mL. Compound **14** was purified by semipreparative HPLC (65% acetonitrile in water) by collecting the peak at 6 min. The decay-corrected radiochemical yield was 10%, and the compound purity was >95%, as assessed by analytical HPLC and coelution with the nonradiolabeled reference standard, **12**.

Radiosynthesis of 2-^{18}F-Ethylbenzoate.—A solution of kryptofix/K^{18}F was received from the cyclotron and transferred into a crimped V-vial for drying. Acetonitrile (0.4 mL) was added to the mixture, which was dried under a stream of argon at 80°C. A solution of 2-nitro ethylbenzoic acid (8 mg, Sigma, Milwaukee, WI) in dry acetonitrile (0.4 mL) was added to the dried kryptofix/K^{18}F, and the mixture was heated to 120°C and stirred under argon for 20 min. The reaction was cooled, passed through a silica-gel cartridge (Alltech, Nicholasville, KY, 900 mg), and eluted with 30% methanol in dichloromethane (2 mL). Afterward, the solvent was evaporated under a stream of argon to a volume <0.5 mL, and the product was purified by semipreparative HPLC. The desired compound was isolated with 50% MeCN in water at 20 min. This product was injected into an analytical HPLC with the authentic nonradiolabeled compound (used as purchased from Sigma, Milwaukee, WI) to assess the identity and purity of the desired compound. The compound was obtained in 8%

radiochemical yield and >95% purity as determined by HPLC. For more details, see the Supporting Information.

Radiosynthesis of 2-^{18}F-Benzaldehyde.—A solution of kryptofix/K18F was received from the cyclotron and transferred into a crimped V-vial for drying. Acetonitrile (0.4 mL) was added to the mixture, and it was dried under a stream of argon at 105°C. A solution of 2-nitrobenzaldehyde (8 mg, Sigma, Milwaukee, WI) in dry DMSO (0.4 mL) was added to the dried kryptofix/K^{18}F, and the mixture was heated to 120°C and stirred under argon for 20 min. The reaction was cooled, passed through a silica-gel cartridge (Alltech, Nicholasville, KY, 900 mg), and eluted with 30% methanol in dichloromethane (2 mL). Afterward, the solvent was evaporated under a stream of argon to a volume <0.5 mL, and the product was purified by semipreparative HPLC. The desired compound was isolated with 50% MeCN in water at 20 min. This product was injected into an analytical HPLC with the authentic nonradiolabeled compound (used as purchased from Sigma, Milwaukee, WI) to assess the identity and purity of the desired compound. The compound was obtained in 11% radiochemical yield and >95% purity as determined by HPLC. For more details, see the Supporting Information.

SIRT-Enzyme Assay.

Recombinant SIRT1−7 enzymes and BPS1 reference substrate for SIRT1, an oligopeptide corresponding to 379−382 of p53 (Arg-His-Lys-Lys(Ac)-AMC) were purchased from BPS Bioscience (San Diego, CA). Solutions (10 mM) of all newly synthesized compounds were prepared in pure DMSO and then diluted to 100 μM aliquots in DMSO for further use. Enzyme-assay reactions were performed in black, low-binding 96-well microtiter plates (Nagle Nunc International, Rochester, NY). End-point assays were performed by incubation of the appropriate substrate, NAD, a SIRT enzyme, and inhibitor (if applicable) in enzyme-assay buffer (50 μL final volume). Control wells without enzyme were included in each plate (Table S1). After 40 min at 37°C, a developer mixture (50 μL) containing nicotinamide (2 mM) and trypsin (0.4 mg mL−1) was added, and the mixtures were incubated for 30 min at 22°C. The intensity of cleaved 7-amino-4-methylcoumarin (AMC) fluorescence was measured using a Synergy H1 microplate reader (Biotek, Winooski, VT) at a 360 nm excitation wavelength and a 450 nm emission wavelength. The maximum excitation wavelengths for this compound are 340−360 nm in ethanol, and the emission-wavelength spectrum is 420−440 nm (Sigma, Milwaukee, WI). Experiments for the determination of enzyme kinetic parameters were performed by incubation of test compounds or the BPS1 reference substrate at different concentrations with NAD^+ and individual SIRT enzymes in an assay buffer (100 μL final volume) at 37°C for different periods of time (5, 10, 20, 30, and 60 min; Table S2), followed by in situ fluorophore cleavage by the addition of a developer mixture (50 μL) containing nicotinamide (2 mM) and trypsin (0.4 mg mL^{-1}). Fluorescence was measured as relative fluorescence units (RFU) at 22°C to determine the initial linear rate, V_0 (RFU min^{-1}), for each concentration. Data were analyzed using GraphPad Prism v6.02 (GraphPad, La Jolla, CA) to afford K_m (μM) and V_{max} (RFU min^{-1}) values. The K_{cat} values were calculated on the basis of the RFU versus AMC-concentration standard curves, and the enzyme purities and concentrations were provided by the manufacturer.

NMR Analysis.

Recombinant SIRT1 (BPS Bioscience, San Diego, CA) was added to a solution of phosphate buffer with 50 μmol of NAD^+ and 20 μmol of 2-FBzAHA with 10% DMSO-d_6. The reaction mixture was incubated at 37°C for 30 min. The reaction mixture was then transferred to an NMR tube, and additional DMSO-d_6 was added to the mixture to provide enough NMR solvent for adequate resolution. The analysis was carried out on a 500 MHz Varian NMR first shimmed for ^{1}H and then run with ^{19}F spectroscopy. Scans were run until peaks could be adequately resolved, and the baseline remained constant.

In Vivo Imaging Studies in Rats.

Animal care and use procedures were carried out in accordance with protocols written under the guidelines of the National Institutes of Health Guide for the Care and Use of Laboratory Animals and approved by the Institutional Animal Care and Use Committee (IACUC) of Wayne State University (protocol #17-06-283).

MR Imaging.

The animals were anesthetized by inhalation of isoflurane (5% in oxygen for induction and 2−2.5% for maintenance). During the imaging procedure, the animals were placed on a heated recirculating-water platform in order to maintain body temperature at 37°C. The animals were held in position using a bite bar and a home- built receive-only surface-coil two-element phased array was placed dorsal to the head, as described elsewhere.[65] Images were acquired using a 7T ClinScan system (Bruker, Coventry, U.K.) operated by a Siemens console with Syngo software (Siemens, Knoxville, TN). A localizing scan was performed and adjustments to head position were made accordingly. Coronal and axial T_2-weighted images were obtained (repetition time, T_R = 3530 ms; echo time, T_E = 38 ms; slice thickness of 0.5 mm; field of view, FOV = 3.2 × 3.2 cm; resolution of 125 μm × 125 μm × 1 mm; matrix of 320 × 320). Images were processed using ImageJ software (Bethesda, MD).

PET-Imaging Procedures in Animals.

Sprague−Dawley rats (200−250 g, n = 3) were anesthetized with 3% isoflurane in oxygen and maintained at 2% isoflurane in oxygen throughout the imaging studies. The body temperature was maintained using electronically controlled heating pad (M2M Imaging, Cleveland, OH) set at 37°C. Anesthetized rats were placed in a stereotactic head holder made of polycarbonate plastic (Kopf, Tujunga, CA) and attached to the bed of the microPET R4 scanner (Siemens, Knoxville, TN) in the supine position with the long axis of the animal parallel to the long axis of the scanner and the brain positioned in the center of the FOV. Each radiotracer (300−500 μCi/animal) was administered in saline via the tail vein in a total volume ≤1.25 mL as a slow bolus injection over a period of 1 min. Dynamic PET images were obtained over 60 min. After PET imaging, the positioning bed with the affixed anesthetized animal was transferred to an Inveon SPECT/CT scanner (Siemens, Knoxville, TN) and CT images and four overlapping frames (2 min each) were acquired covering the whole body using X-ray-tube settings of 80 kV and 500 μA with an exposure time of 300−350 ms for each of the 360 rotational steps.

Image Analysis and Quantification.

Dynamic PET data sets were truncated into multiple 1−2 min static frames, and images were reconstructed using the two-dimensional-ordered-subsets-expectation-maximization (2DOSEM) algorithm with 4 iterations and 16 subsets, as described before;[19] CT images were reconstructed using the Shepp−Logan algorithm.[66] PET−CT image fusion was accomplished using the Inveon Research Workplace version 3.0 software package (Siemens, Knoxville, TN). PET−CT and T_2-weighted MR images of individual rat heads were manually coregistered using scull landmarks as fiducial markers in AMIDE 1.0.4 software (http://amide.sourceforge.net). The digital rat-brain atlas was used for the identification of specific structures of the brain and manual segmentation of T_2-weighted MR images on the basis of stereotactic coordinates.[67] Radioactivity concentrations in specific brain structures were quantified with AMIDE 1.0.4 software (http://amide.sourceforge.net) using regions-of-interest (ROI) analysis and expressed as microcuries per gram and standard uptake values (SUVs). The SUV is defined as the ratio of the tissue radioactivity concentration, C (in μCi per gram of tissue), at a given time point postinjection, T, to the injected dose (in μCi, decay-corrected to the same time T) normalized by the body weight in grams. Time-activity curves (TAC) for different brain structures were plotted over time after radiotracer administration. Patlak graphical analysis with reference a tissue[36] was used for quantitative analysis of the dynamic PET images with 2-[^{18}F]BzAHA. The brainstem was used as the reference tissue because of its low levels of SIRT1 activity and the subsequent low levels of 2-[^{18}F]BzAHA-derived-radioactivity accumulation in this region of the brain. The brainstem also receives levels of perfusion similar to those of the rest of the brain tissue, thus providing a suitable reference tissue.

Autoradiography.

After PET imaging (or at 25 min after 300−500 μCi radiotracer iv injection), the animals were sacrificed, and the brains were rapidly extracted, frozen, and embedded in mounting medium M1 (Shandon-Lipshaw, Pittsburgh, PA). Serial 20 μm thick coronal sections of frozen brain tissue were obtained at −13°C using a cryo-microtome CM3050S (Leica, Wetzlar, Germany). Tissue sections were thaw-mounted on poly-A-lysine-coated glass slides and heat-fixed for 5 min at 65°C on a slide warmer (Fisher Scientific, Pittsburgh, PA). Tissue sections were mounted on slides and exposed to single-emulsion Carestream Kodak BioMax MR film (8 × 10 in., Sigma, Milwaukee, WI), without exposure to light, in cassettes for 12 h. After tissue exposure, processing of the film was performed by an automated system (Kodak X-Omat, Center for Molecular Medicine and Genetics, Wayne State University).

Arterio-Venous Shunt for Blood Sampling and Analyses of Radiolabeled Metabolites.

An arteriovenous shunt was constructed by inserting two 20 cm long, PE50 catheters into the ends of 6 cm long, thick-walled, Masterflex Tygon L/S 13 silicone tubing (#96400–13; Cole-Parmer, Vernon Hills, IL) and filled by a saline solution containing 10 U/mL heparin (PosiFlush; Beckton-Dickinson, San Jose, CA). Male Sprague−Dawley rats (n = 3) weighing 400−500 g (Envigo, Indianapolis, IN) were anesthetized by inhalation of isoflurane (5% in oxygen for induction and 2−2.5% for maintenance), their lower abdominal and inguinal fur was shaved, and using a scalpel, two 3 cm long skin incisions were made in the inguinal

regions along the edge of the m. obliquus externus abdominis. The subcutaneous tissues and inguinal fascia were spread apart using microforceps, and a wound retractor was placed between the femoral ligament and the m. vastus medialis to reveal the femoral canal. Connective tissue and fascial layer covering the femoral neurovascular bundle were opened using a 90° hook, and the femoral artery and femoral vein were separated from surrounding tissues and lifted on 3/0 silk threads to stop the blood flow. A small incision in the wall of the femoral artery was made one-third of the arterial diameter at a 45° angle using microscissors. One end of the shunt (PE50 catheter) was introduced into the arterial lumen and fixed by proximal and distal 3/0 silk knots, and blood flow from the femoral artery was verified. Then, a small incision was made in the wall of the femoral vein, and the other end of the clamped shunt was introduced into the femoral-vein lumen and fixed by proximal and distal 3/0 silk knots. The shunt was unclamped to enable the blood flow from the femoral artery into the femoral vein; the shunt was flushed by an injection of 0.5 mL of saline solution containing 10 U/mL heparin (PosiFlush; Beckton-Dickinson, San Jose, CA) using a 1 mL insulin syringe with a short 30 Ga hypodermic needle inserted into the thick-walled segment of the shunt. The contralateral femoral vein was catheterized using a PE50 catheter through the contralateral skin incision using similar surgical steps. Intravenous administration of the radiotracer was performed using a PDH Ultra digital syringe-injection pump (Harvard Apparatus, Holliston, MA) at a rate of 1 mL/min (1 mL total volume of injectate). Serial arterial blood samples (100 μL each) were obtained at different time points after radiotracer administration (at 1, 5, 10, 15, 30, 45, 60, and 90 min) using heparinized 1 mL syringes with 30 Ga hypodermic needles inserted into the thick-walled segment of the shunt, compressed on the venous end to prevent sampling of venous blood. Each blood sample was centrifuged at 1000g for 5 min in heparinized 2.5 mL plastic vials to obtain blood plasma, and the aqueous fraction was separated from plasma proteins by centrifugation through a 1 mL Ultrafiltration Centrifugal Filter 4101 (Millipore/EDM, Billerica, MA). The aqueous fraction of the plasma was analyzed without any additional extraction procedures using a radio-HPLC system and a mobile phase as described for the quality control of 2-[^{18}F]BzAHA radiosynthesis.

Histology and Immunofluorescence Microscopy.

Male Sprague−Dawley rats (Envigo) were anesthetized using sodium pentobarbital (50 mg/kg) and transcardially perfused with 4% formaldehyde in phosphate buffer. After fixation in 4% formaldehyde and 30% sucrose, coronal brain sections (20 μm) were obtained using OTF5000 cryomicrotome (Hacker-Bright Instruments, Winnsboro, SC) and set up as floating sections in buffered saline. For fluorescence immunohistochemistry of SIRT1, the sections were washed in PBS with triton detergent (PBS-T, 0.1 M, pH 7.4; 3 × 3 min); this was followed by antigen retrieval at 70°C in sodium citrate buffer (pH 6.0) for 1 h and then three washes in PBS-T (3 × 3 min). The sections were heated for 5 min at 55°C, washed with xylenes three times for 2 min each, then rinsed in PBS (3 × 3 min). The sections were then incubated in 5% normal goat serum for 20 min at 20°C. Immediately following this, the sections were washed three times in PBS-T and set up for an 18 h incubation at 4°C in primary AlexaFluor488-conjugated anti-SIRT1 mouse monoclonal antibody (1:200, catalogue no. ab157401; Abcam, Cambridge, U.K.). Following incubation, the antibody was removed, and the sections were washed in PBS-T three times. The sections were mounted on

high-tissue-binding Superfrost Plus glass slides (Fisher Scientific, Waltham, MA) and coverslipped using an aqueous medium containing DAPI for the nuclear stain (Vectashield; Vector Laboratories, Burlingame, CA). Select sections were dual-immunostained using the rabbit anti-phospho-SIRT1 monoclonal antibody S47 (1:200, catalogue no. ab76039; Abcam, Cambridge, U.K.) incubated for 14 h at 4°C; this was followed by three 2 min washes in TBS and exposure to the secondary goat antirabbit polyclonal antibody conjugated to AlexaFluor647 (1:250, catalogue no. ab150079; Abcam, Cambridge, U.K.) for 90 min at 4°C. Following three 2 min washes in TBS, the sections were mounted and coverslipped as described above. Fluorescence-microscopy images were acquired using EVOS FL Auto (Life Technologies, Carlsbad, CA).

Statistical Analyses.

Excel 2010 (Microsoft, Redmond, WA) and Graph-Pad Prism 6 (Graph Pad Software, La Jolla, CA) were used for calculations and statistical analyses of data. Data are reported as means ± standard deviations. Student's t test for group mean and paired measurements was used to calculate P values. An $\alpha = 0.05$ was considered to indicate a significant difference, and a two-tailed distribution was assumed. $P < 0.05$ was considered as statistically significant.

Supplementary Material

Refer to Web version on PubMed Central for supplementary material.

ACKNOWLEDGMENTS

We would like to acknowledge funding support from the NIH via an R01 grant (R01DA03033) to J.G. and from the Core Center Support Grant (P30 CA022453), which supports the Small Animal Imaging Core of Karmanos Cancer Institute, Detroit, MI.

ABBREVIATIONS USED

Acb	nucleus accumbens
AHA	aminohexanoicanilide
AMC	7-amino-4-methylcoumarin
Bz	benzoyl
DG	dentate gyrus
eNOS	endothelial nitric oxide
HDAC	histone deacetylase
HIF1a	hypoxia-inducible factor 1a
IFM	immunofluorescence microscopy
LC	locus coeruleus

LS	lateral septal nucleus
MMP1	metallo-metalprotease
SIRT	sirtuin
NAD	nicotinic adenine dinucleotide
PhAc	phenyl acetyl
VEGF	vascular-endothelial-growth factor

REFERENCES

(1). Michan S; Sinclair D Sirtuins in mammals: insights into their biological function. Biochem. J 2007, 404 (1), 1–13. [PubMed: 17447894]

(2). (a)Haberland M; Montgomery RL; Olson EN The many roles of histone deacetylases in development and physiology: implications for disease and therapy. Nat. Rev. Genet 2009, 10 (1), 32–42. [PubMed: 19065135] (b)Costantini S; Sharma A; Raucci R; Costantini M; Autiero I; Colonna G Genealogy of an ancient protein family: the Sirtuins, a family of disordered members. BMC Evol. Biol 2013, 13,60. [PubMed: 23497088]

(3). (a)Giannakou ME; Partridge L The interaction between FOXO and SIRT1: tipping the balance towards survival. Trends Cell Biol 2004, 14 (8), 408–412. [PubMed: 15308206] (b)Howitz KT; Bitterman KJ; Cohen HY; Lamming DW; Lavu S; Wood JG; Zipkin RE; Chung P; Kisielewski A; Zhang LL; Scherer B; Sinclair DA Small molecule activators of sirtuins extend Saccharomyces cerevisiae lifespan. Nature 2003, 425 (6954), 191–196. [PubMed: 12939617] (c)Mouchiroud L; Houtkooper RH; Moullan N; Katsyuba E; Ryu D; Canto C; Mottis A; Jo YS; Viswanathan M; Schoonjans K; Guarente L; Auwerx J The NAD(+)/sirtuin pathway modulates longevity through activation of mitochondrial UPR and FOXO signaling. Cell 2013, 154 (2), 430–441. [PubMed: 23870130]

(4). Pan PW; Feldman JL; Devries MK; Dong A; Edwards AM; Denu JM Structure and biochemical functions of SIRT6. J. Biol. Chem 2011, 286 (16), 14575–14587. [PubMed: 21362626]

(5). Lin Z; Fang D The roles of SIRT1 in cancer. Genes Cancer 2013, 4 (3–4), 97–104. [PubMed: 24020000]

(6). (a)Nogueiras R; Habegger KM; Chaudhary N; Finan B; Banks AS; Dietrich MO; Horvath TL; Sinclair DA; Pfluger PT; Tschöp MH Sirtuin 1 and sirtuin 3: physiological modulators of metabolism. Physiol. Rev 2012, 92 (3), 1479–1514. [PubMed: 22811431] (b)Baksi A; Kraydashenko O; Zalevkaya A; Stets R; Elliott P; Haddad J; Hoffmann E; Vlasuk GP; Jacobson EW A phase II, randomized, placebo-controlled, double-blind, multi-dose study of SRT2104, a SIRT1 activator, in subjects with type 2 diabetes. British journal of clinical pharmacology 2014, 78 (1), 69–77. [PubMed: 24446723] (c)Kitada M; Koya D SIRT1 in type 2 diabetes: mechanisms and therapeutic potential. Diabetes & metabolism journal 2013, 37 (5), 315–325. [PubMed: 24199159]

(7). Matsushima S; Sadoshima J The role of sirtuins in cardiac disease. American journal of physiology. Heart and circulatory physiology 2015, 309 (9), H1375–H1389. [PubMed: 26232232]

(8). (a)Haigis MC; Sinclair DA Mammalian sirtuins: biological insights and disease relevance. Annu. Rev. Pathol.: Mech. Dis 2010, 5, 253–295.(b)Donmez G; Outeiro TF SIRT1 and SIRT2: emerging targets in neurodegeneration. EMBO molecular medicine 2013, 5 (3), 344–352. [PubMed: 23417962]

(9). (a)Barber MF; Michishita-Kioi E; Xi Y; Tasselli L; Kioi M; Moqtaderi Z; Tennen RI; Paredes S; Young NL; Chen K; Struhl K; Garcia BA; Gozani O; Li W; Chua KF SIRT7 links H3K18 deacetylation to maintenance of oncogenic transformation. Nature 2012, 487 (7405), 114–118. [PubMed: 22722849] (b)Bheda P; Jing H; Wolberger C; Lin H The substrate specificity of sirtuins. Annu. Rev. Biochem 2016, 85, 405–429. [PubMed: 27088879]

(10). (a)Pulla VK; Battu MB; Alvala M; Sriram D; Yogeeswari P Can targeting SIRT-1 to treat type 2 diabetes be a good strategy? A review. Expert Opin. Ther. Targets 2012, 16 (8), 819–832. [PubMed: 22762724] (b)Poulsen MM; Vestergaard PF; Clasen BF; Radko Y; Christensen LP; Stødkilde-Jørgensen H; Møller N; Jessen N; Pedersen SB; Jørgensen JOL High-dose resveratrol supplementation in obese men: an investigator-initiated, randomized, placebo-controlled clinical trial of substrate metabolism, insulin sensitivity, and body composition. Diabetes 2013, 62 (4), 1186–1195. [PubMed: 23193181] (c)Hoffmann G; Breitenbücher F; Schuler M; Ehrenhofer-Murray AE A novel sirtuin 2 (SIRT2) inhibitor with p53-dependent pro-apoptotic activity in non-small cell lung cancer. J. Biol. Chem 2014, 289 (8), 5208–5216. [PubMed: 24379401]

(11). (a)Napper AD; Hixon J; McDonagh T; Keavey K; Pons J-F; Barker J; Yau WT; Amouzegh P; Flegg A; Hamelin E; Thomas RJ; Kates M; Jones S; Navia MA; Saunders JO; DiStefano PS; Curtis R Discovery of indoles as potent and selective inhibitors of the deacetylase SIRT1. J. Med. Chem 2005, 48 (25), 8045–8054. [PubMed: 16335928] (b)Solomon JM; Pasupuleti R; Xu L; McDonagh T; Curtis R; DiStefano PS; Huber LJ Inhibition of SIRT1 catalytic activity increases p53 acetylation but does not alter cell survival following DNA damage. Mol. Cell. Biol 2006, 26 (1), 28–38. [PubMed: 16354677]

(12). Grozinger CM; Chao ED; Blackwell HE; Moazed D; Schreiber SL Identification of a class of small molecule inhibitors of the sirtuin family of NAD-dependent deacetylases by phenotypic screening. J. Biol. Chem 2001, 276 (42), 38837–38843. [PubMed: 11483616]

(13). Lain S; Hollick JJ; Campbell J; Staples OD; Higgins M; Aoubala M; McCarthy A; Appleyard V; Murray KE; Baker L; et al. Discovery, in vivo activity, and mechanism of action of a small-molecule p53 activator. Cancer Cell 2008, 13 (5), 454–463. [PubMed: 18455128]

(14). (a)Liu T; Liu PY; Marshall GM The critical role of the class III histone deacetylase SIRT1 in cancer. Cancer Res 2009, 69 (5), 1702–1705. [PubMed: 19244112] (b)Knight JR; Milner J SIRT1, metabolism and cancer. Curr. Opin. Oncol 2012, 24 (1), 68–75. [PubMed: 22080944]

(15). (a)Wong SY; Tang BL SIRT1 as a therapeutic target for Alzheimer's disease. Rev. Neurosci 2016, 27 (8), 813–825. [PubMed: 27497424] (b)Nimmagadda VK; Makar TK; Chandrasekaran K; Sagi AR; Ray J; Russell JW; Bever CT, Jr. SIRT1 and NAD+ precursors: therapeutic targets in multiple sclerosis a review. J. Neuroimmunol 2016, 304 (3), 29–34. [PubMed: 27474445] (c)Ajami M; Pazoki-Toroudi H; Amani H; Nabavi SF; Braidy N; Vacca RA; Atanasov AG; Mocan A; Nabavi SM Therapeutic role of sirtuins in neurodegenerative disease and their modulation by polyphenols. Neurosci. Biobehav. Rev 2017, 73 (2), 39–47. [PubMed: 27914941] (d)Liu Z; Yang T; Li X; Peng T; Hang HC; Li XD Integrative chemical biology approaches for identification and characterization of "erasers" for fatty-acid-acylated lysine residues within proteins. Angew. Chem., Int. Ed 2015, 54 (4), 1149–1152.(e)Sussmuth SD; Haider S; Landwehrmeyer GB; Farmer R; Frost C; Tripepi G; Andersen CA; Di Bacco M; Lamanna C; Diodato E; Massai L; Diamanti D; Mori E; Magnoni L; Dreyhaupt J; Schiefele K; Craufurd D; Saft C; Rudzinska M; Ryglewicz D; Orth M; Brzozy S; Baran A; Pollio G; Andre R; Tabrizi SJ; Darpo B; Westerberg G An exploratory double-blind, randomized clinical trial with selisistat, a Sirt1 inhibitor, in patients with huntington's disease. British journal of clinical pharmacology 2015, 79 (3), 465–476. [PubMed: 25223731]

(16). (a)Vigili de Kreutzenberg S; Ceolotto G; Cattelan A; Pagnin E; Mazzucato M; Garagnani P; Borelli V; Bacalini MG; Franceschi C; Fadini GP; Avogaro A Metformin improves putative longevity effectors in peripheral mononuclear cells from subjects with prediabetes. A randomized controlled trial. Nutr., Metab. Cardiovasc. Dis 2015, 25 (7), 686–693. [PubMed: 25921843] (b)Xu W; Deng YY; Yang L; Zhao S; Liu J; Zhao Z; Wang L; Maharjan P; Gao S; Tian Y; Zhuo X; Zhao Y; Zhou J; Yuan Z; Wu Y Metformin ameliorates the proinflammatory state in patients with carotid artery atherosclerosis through sirtuin 1 induction. Translational research: the journal of laboratory and clinical medicine 2015, 166 (5), 451–458. [PubMed: 26141671] (c)Goh KP; Lee HY; Lau DP; Supaat W; Chan YH; Koh AF Effects of resveratrol in patients with type 2 diabetes mellitus on skeletal muscle SIRT1 expression and energy expenditure. Int. J. Sport Nutr. Exercise Metab 2014, 24 (1), 2–13.(d)Lopez-Domenech S; Banuls C; de Maranon AM; Abab-Jimenez Z; Morillas C; Gomez-Abril SA; Rovira-Llopis S; Victor VM; Hernandez-Mijares A; Rocha M Pinitol alleviates systemic inflammatory cytokines in human obesity by a mechanism involving unfolded protein response and sirtuin 1. Clin. Nutr 2017, 36 (5), 1–9.(e)Nakamura K; Kageyama S; Ke B; Fujii T; Sosa RA; Reed EF; Datta N; Zarrinpar A; Busuttil RW; Kupiec-

Weglinski JW Sirtuin 1 attenuates inflammation and hepatocellular damage in liver transplant ischemia/reperfusion: from mouse to human. Liver transplantation 2017, 23 (10), 1282–1293. [PubMed: 28719070]

(17). Borra MT; Langer MR; Slama JT; Denu JM Substrate specificity and kinetic mechanism of the Sir2 family of NAD +-dependent histone/protein deacetylases. Biochemistry 2004, 43 (30), 9877–9887. [PubMed: 15274642]

(18). Yeh H-H; Tian M; Hinz R; Young D; Shavrin A; Mukhapadhyay U; Flores LG; Balatoni J; Soghomonyan S; Jeong HJ; Pal A; Uthamanthil R; Jackson JN; Nishii R; Mizuma H; Onoe H; Kagawa S; Higashi T; Fukumitsu N; Alauddin M; Tong W; Herholz K; Gelovani JG Imaging epigenetic regulation by histone deacetylases in the brain using PET/MRI with 18F-FAHA. NeuroImage 2013, 64 (0), 630–639. [PubMed: 22995777]

(19). Bonomi R; Mukhopadhyay U; Shavrin A; Yeh H-H; Majhi A; Dewage SW; Najjar A; Lu X; Cisneros GA; Tong WP; Alauddin MM; Liu R-S; Mangner TJ; Turkman N; Gelovani JG Novel histone deacetylase class IIa selective substrate radiotracers for PET imaging of epigenetic regulation in the brain. PLoS One 2015, 10 (8), e0133512. [PubMed: 26244761]

(20). Hirsch BM; Zheng W Sirtuin mechanism and inhibition: explored with N(epsilon)-acetyl-lysine analogs. Mol. BioSyst 2011, 7 (1), 16–28. [PubMed: 20842312]

(21). (a)Yeh HH; Tian M; Hinz R; Young D; Shavrin A; Mukhapadhyay U; Flores LG; Balatoni J; Soghomonyan S; Jeong HJ; Pal A; Uthamanthil R; Jackson JN; Nishii R; Mizuma H; Onoe H; Kagawa S; Higashi T; Fukumitsu N; Alauddin M; Tong W; Herholz K; Gelovani JG Imaging epigenetic regulation by histone deacetylases in the brain using PET/MRI with ^{18}F-FAHA. NeuroImage 2013, 64, 630–639. [PubMed: 22995777] (b)Reid AE; Hooker J; Shumay E; Logan J; Shea C; Kim SW; Collins S; Xu Y; Volkow N; Fowler JS Evaluation of 6-([^{18}F]-fluoroacetamido)-1-hexanoicanilide for PET imaging of histone deacetylase in the baboon brain. Nucl. Med. Biol 2009, 36 (3), 247–258. [PubMed: 19324270] (c)Sanabria SM; Fan H; Riffel K; Williams M; Ryan C; Gibson R; Gelovani J; Cook J; Hostetler E Quantification of HDAC inhibition by F-SAHA in rhesus monkey brain using the PET tracer [^{18}F] FAHA. NeuroImage 2008, 41, T15.

(22). Wey HY; Wang C; Schroeder FA; Logan J; Price JC; Hooker JM Kinetic analysis and quantification of [^{11}C]martinostat for in vivo HDAC imaging of the brain. ACS Chem. Neurosci 2015, 6 (5), 708–715. [PubMed: 25768025]

(23). Strebl MG; Wang C; Schroeder FA; Placzek MS; Wey HY; Van de Bittner GC; Neelamegam R; Hooker JM Development of a fluorinated class-I HDAC radiotracer reveals key chemical determinants of brain penetrance. ACS Chem. Neurosci 2016, 7 (5), 528–533. [PubMed: 26675505]

(24). Wey HY; Gilbert TM; Zurcher NR; She A; Bhanot A; Taillon BD; Schroeder FA; Wang C; Haggarty SJ; Hooker JM Insights into neuroepigenetics through human histone deacetylase PET imaging. Sci. Transl. Med 2016, 8 (351), 351ra106.

(25). Wang C; Schroeder FA; Wey HY; Borra R; Wagner FF; Reis S; Kim SW; Holson EB; Haggarty SJ; Hooker JM In vivo imaging of histone deacetylases (HDACs) in the central nervous system and major peripheral organs. J. Med. Chem 2014, 57 (19), 7999–8009. [PubMed: 25203558]

(26). Maurer B; Rumpf T; Scharfe M; Stolfa DA; Schmitt ML; He W; Verdin E; Sippl W; Jung M Inhibitors of the NAD^+-dependent protein desuccinylase and demalonylase Sirt5. ACS Med. Chem. Lett 2012, 3 (12), 1050–1053. [PubMed: 24900427]

(27). Wu J; Zhang D; Chen L; Li J; Wang J; Ning C; Yu N; Zhao F; Chen D; Chen X; Chen K; Jiang H; Liu H; Liu D Discovery and mechanism study of SIRT1 activators that promote the deacetylation of fluorophore-labeled substrate. J. Med. Chem 2013, 56 (3), 761–780. [PubMed: 23316803]

(28). Toro TB; Bryant JR; Watt TJ Lysine deacetylases exhibit distinct changes in activity profiles due to fluorophore-conjugation of substrates. Biochemistry 2017, 56 (34), 4549–4558. [PubMed: 28749131]

(29). (a)Du J; Zhou Y; Su X; Yu JJ; Khan S; Jiang H; Kim J; Woo J; Kim JH; Choi BH; He B; Chen W; Zhang S; Cerione RA; Auwerx J; Hao Q; Lin H Sirt5 is a NAD-dependent protein lysine demalonylase and desuccinylase. Science (Washington, DC, U. S.) 2011, 334 (6057), 806–809. (b)He B; Hu J; Zhang X; Lin H Thiomyristoyl peptides as cell-permeable Sirt6 inhibitors. Org.

Biomol. Chem 2014, 12 (38), 7498–7502. [PubMed: 25163004] (c)Heltweg B; Brauch C; Jung M; Dequiedt F; Marshall BL; Verdin E; Yoshida M; Nishino N Subtype selective substrates for histone deacetylases. J. Med. Chem 2004, 47 (21), 5235–5243. [PubMed: 15456267] (d)Mathias RA; Greco TM; Oberstein A; Budayeva HG; Chakrabarti R; Rowland EA; Kang Y; Shenk T; Cristea IM Sirtuin 4 Is a lipoamidase regulating pyruvate dehydrogenase complex activity. Cell 2014, 159 (7), 1615–1625. [PubMed: 25525879]

(30). Tredwell M; Preshlock SM; Taylor NJ; Gruber S; Huiban M; Passchier J; Mercier J; Genicot C; Gouverneur V A general copper-mediated nucleophilic 18F fluorination of arenes. Angew. Chem., Int. Ed 2014, 53 (30), 7751–7755.

(31). McCammant MS; Thompson S; Brooks AF; Krska SW; Scott PJH; Sanford MS Cu-Mediated C −H ^{18}F-fluorination of electron-rich (hetero)arenes. Org. Lett 2017, 19 (14), 3939–3942. [PubMed: 28665619]

(32). Shen B; Ehrlichmann W; Uebele M; Machulla HJ; Reischl G Automated synthesis of n.c.a. [^{18}F]FDOPA via nucleophilic aromatic substitution with [^{18}F]fluoride. Appl. Radiat. Isot 2009, 67 (9), 1650–1653. [PubMed: 19433364]

(33). (a)Wang M; Gao M; Miller KD; Sledge GW; Zheng Q-H [^{11}C]GSK2126458 and [^{18}F]GSK2126458, the first radiosyn-thesis of new potential PET agents for imaging of PI3K and mTOR in cancers. Bioorg. Med. Chem. Lett 2012, 22 (4), 1569–1574. [PubMed: 22297110] (b)Shen B; Ehrlichmann W; Uebele M; Machulla HJ; Reischl G Automated synthesis of n.c.a. [^{18}F]FDOPA via nucleophilic aromatic substitution with [^{18}F]fluoride. Appl. Radiat. Isot 2009, 67 (9), 1650–1653. [PubMed: 19433364]

(34). Feldman JL; Dittenhafer-Reed KE; Denu JM Sirtuin catalysis and regulation. J. Biol. Chem 2012, 287 (51), 42419–42427. [PubMed: 23086947]

(35). Mashimo M; Kato J; Moss J Structure and function of the ARH family of ADP-ribose-acceptor hydrolases. DNA Repair 2014, 23, 88–94. [PubMed: 24746921]

(36). Patlak CS; Blasberg RG Graphical evaluation of blood-to-brain transfer constants from multiple-time uptake data. Generalizations. J. Cereb. Blood Flow Metab 1985, 5 (4), 584–590. [PubMed: 4055928]

(37). Patlak CS; Blasberg RG; Fenstermacher JD Graphical evaluation of blood-to-brain transfer constants from multiple-time uptake data. J. Cereb. Blood Flow Metab 1983, 3 (1), 1–7. [PubMed: 6822610]

(38). (a)Ramadori G; Lee CE; Bookout AL; Lee S; Williams KW; Anderson J; Elmquist JK; Coppari R Brain SIRT1: anatomical distribution and regulation by energy availability. J. Neurosci 2008, 28 (40), 9989–9996. [PubMed: 18829956] (b)Zakhary SM; Ayubcha D; Dileo JN; Jose R; Leheste JR; Horowitz JM; Torres G Distribution analysis of deacetylase SIRT1 in rodent and human nervous systems. Anat. Rec 2010, 293 (6), 1024–1032.

(39). Michan S; Li Y; Chou MM; Parrella E; Ge H; Long JM; Allard JS; Lewis K; Miller M; Xu W; Mervis RF; Chen J; Guerin KI; Smith LE; McBurney MW; Sinclair DA; Baudry M; de Cabo R; Longo VD SIRT1 is essential for normal cognitive function and synaptic plasticity. J. Neurosci 2010, 30 (29), 9695–9707. [PubMed: 20660252]

(40). Ng F; Wijaya L; Tang BL SIRT1 in the brain—connections with aging-associated disorders and lifespan. Front. Cell. Neurosci 2015, 9, 64. [PubMed: 25805970]

(41). Saharan S; Jhaveri DJ; Bartlett PF SIRT1 regulates the neurogenic potential of neural precursors in the adult subventricular zone and hippocampus. J. Neurosci. Res 2013, 91 (5), 642–659. [PubMed: 23404532]

(42). Moorthi P; Premkumar P; Priyanka R; Jayachandran KS; Anusuyadevi M Pathological changes in hippocampal neuronal circuits underlie age-associated neurodegeneration and memory loss: positive clue toward SAD. Neuroscience 2015, 301, 90–105. [PubMed: 26045180]

(43). Braidy N; Poljak A; Grant R; Jayasena T; Mansour H; Chan-Ling T; Smythe G; Sachdev P; Guillemin GJ Differential expression of sirtuins in the aging rat brain. Front. Cell. Neurosci 2015, 9, 167–183. [PubMed: 26005404]

(44). Abe-Higuchi N; Uchida S; Yamagata H; Higuchi F; Hobara T; Hara K; Kobayashi A; Watanabe Y Hippocampal sirtuin 1 signaling mediates depression-like behavior. Biol. Psychiatry 2016, 80 (11), 815–826. [PubMed: 27016384]

(45). Lutz MI; Milenkovic I; Regelsberger G; Kovacs GG Distinct patterns of sirtuin expression during progression of Alzheimer's disease. NeuroMol. Med 2014, 16 (2), 405–414.

(46). Heyward FD; Gilliam D; Coleman MA; Gavin CF; Wang J; Kaas G; Trieu R; Lewis J; Moulden J; Sweatt JD Obesity weighs down memory through a mechanism involving the neuroepigenetic dysregulation of Sirt1. J. Neurosci 2016, 36 (4), 1324–1335. [PubMed: 26818519]

(47). Smith MR; Syed A; Lukacsovich T; Purcell J; Barbaro BA; Worthge SA; Wei SR; Pollio G; Magnoni L; Scali C; Massai L; Franceschini D; Camarri M; Gianfriddo M; Diodato E; Thomas R; Gokce O; Tabrizi SJ; Caricasole A; Landwehrmeyer B; Menalled L; Murphy C; Ramboz S; Luthi-Carter R; Westerberg G; Marsh JL A potent and selective Sirtuin 1 inhibitor alleviates pathology in multiple animal and cell models of Huntington's disease. Hum. Mol. Genet 2014, 23 (11), 2995–3007. [PubMed: 24436303]

(48). Naia L; Rego AC Sirtuins: double players in Huntington's disease. Biochim. Biophys. Acta, Mol. Basis Dis 2015, 1852, 2183–2194.

(49). (a)Ferguson D; Shao N; Heller E; Feng J; Neve R; Kim HD; Call T; Magazu S; Shen L; Nestler EJ SIRT1-FOXO3a regulate cocaine actions in the nucleus accumbens. J. Neurosci 2015, 35 (7), 3100–3111. [PubMed: 25698746] (b)Wang X; Hu S; Liu L Phosphorylation and acetylation modifications of FOXO3a: Independently or synergistically? Oncol. Lett 2017, 13 (5), 2867–2872. [PubMed: 28521392]

(50). Renthal W; Kumar A; Xiao G; Wilkinson M; Covington HE, 3rd; Maze I; Sikder D; Robison AJ; LaPlant Q; Dietz DM; Russo SJ; Vialou V; Chakravarty S; Kodadek TJ; Stack A; Kabbaj M; Nestler EJ Genome-wide analysis of chromatin regulation by cocaine reveals a role for sirtuins. Neuron 2009, 62 (3), 335–348. [PubMed: 19447090]

(51). Cakir I; Perello M; Lansari O; Messier NJ; Vaslet CA; Nillni EA Hypothalamic Sirt1 regulates food intake in a rodent model system. PLoS One 2009, 4 (12), e8322. [PubMed: 20020036]

(52). Ramadori G; Fujikawa T; Fukuda M; Anderson J; Morgan DA; Mostoslavsky R; Stuart RC; Perello M; Vianna CR; Nillni EA; Rahmouni K; Coppari R SIRT1 deacetylase in POMC neurons is required for homeostatic defenses against diet-induced obesity. Cell Metab 2010, 12 (1), 78–87. [PubMed: 20620997]

(53). Choi Y-H; Fujikawa T; Lee J; Reuter A; Kim KW Revisiting the ventral medial nucleus of the hypothalamus: the roles of SF-1 neurons in energy homeostasis. Frontiers in Neuroscience 2013, 7 (71), 1–9. [PubMed: 23386807]

(54). Coppari R Metabolic actions of hypothalamic SIRT1. Trends Endocrinol. Metab 2012, 23 (4), 179–185. [PubMed: 22382036]

(55). Susanti VY; Sasaki T; Yokota-Hashimoto H; Matsui S; Lee YS; Kikuchi O; Shimpuku M; Kim HJ; Kobayashi M; Kitamura T Sirt1 rescues the obesity induced by insulin-resistant constitutively-nuclear FoxO1 in POMC neurons of male mice. Obesity 2014, 22 (10), 2115–2119. [PubMed: 25044690]

(56). Bonkowski MS; Sinclair DA Slowing ageing by design: the rise of NAD^+ and sirtuin-activating compounds. Nat. Rev. Mol. Cell Biol 2016, 17 (11), 679–690. [PubMed: 27552971]

(57). Panossian L; Fenik P; Zhu Y; Zhan G; McBurney MW; Veasey S SIRT1 regulation of wakefulness and senescence-like phenotype in wake neurons. J. Neurosci 2011, 31 (11), 4025–4036. [PubMed: 21411645]

(58). Kenworthy CA; Sengupta A; Luz SM; Ver Hoeve ES; Meda K; Bhatnagar S; Abel T Social defeat induces changes in histone acetylation and expression of histone modifying enzymes in the ventral hippocampus, prefrontal cortex, and dorsal raphe nucleus. Neuroscience 2014, 264, 88–98. [PubMed: 23370319]

(59). Logan J; Fowler JS; Volkow ND; Wang GJ; Ding YS; Alexoff DL Distribution volume ratios without blood sampling from graphical analysis of PET data. J. Cereb. Blood Flow Metab 1996, 16, 834–840. [PubMed: 8784228]

(60). Hattori Y; Okamoto Y; Maki T; Yamamoto Y; Oishi N; Yamahara K; Nagatsuka K; Takahashi R; Kalaria RN; Fukuyama H; Kinoshita M; Ihara M Silent Information regulator 2 homolog 1 counters cerebral hypoperfusion injury by deacetylating endothelial nitric oxide synthase. Stroke 2014, 45 (11), 3403–3411. [PubMed: 25213338]

(61). Della-Morte D; Dave KR; DeFazio RA; Bao YC; Raval AP; Perez-Pinzon MA Resveratrol pretreatment protects rat brain from cerebral ischemic damage via a sirtuin 1−uncoupling protein 2 pathway. Neuroscience 2009, 159 (3), 993–1002. [PubMed: 19356683]

(62). Joo HY; Yun M; Jeong J; Park ER; Shin HJ; Woo SR; Jung JK; Kim YM; Park JJ; Kim J; Lee KH SIRT1 deacetylates and stabilizes hypoxia-inducible factor-1alpha (HIF-1α) via direct interactions during hypoxia. Biochem. Biophys. Res. Commun 2015, 462 (4), 294–300. [PubMed: 25979359]

(63). Mukhopadhyay U; Tong WP; Gelovani JG; Alauddin MM Radiosynthesis of 6-([^{18}F]fluoroacetamido)-1-hexanoicanilide ([^{18}F]FAHA) for PET imaging of histone deacetylase (HDAC). J. Labelled Compd. Radiopharm 2006, 49 (11), 997–1006.

(64). Heltweg B; Dequiedt F; Verdin E; Jung M Nonisotopic substrate for assaying both human zinc and NAD^+-dependent histone deacetylases. Anal. Biochem 2003, 319 (1), 42–48. [PubMed: 12842105]

(65). (a)Bissig D; Berkowitz BA Same-session functional assessment of rat retina and brain with manganese-enhanced MRI. NeuroImage 2011, 58 (3), 749–760. [PubMed: 21749922] (b)Yacoub E; Shmuel A; Pfeuffer J; Van De Moortele PF; Adriany G; Andersen P; Vaughan JT; Merkle H; Ugurbil K; Hu X Imaging brain function in humans at 7 T. Magn. Reson. Med 2001, 45 (4), 588–594. [PubMed: 11283986]

(66). Shepp LA; Logan BF The Fourier reconstruction of a head section. IEEE Trans. Nucl. Sci 1974, 21 (3), 21–43.

(67). Watson GP C. The Rat Brain in Stereotaxic Coordinates, 6thed.; Academic Press: San Diego, 2006.

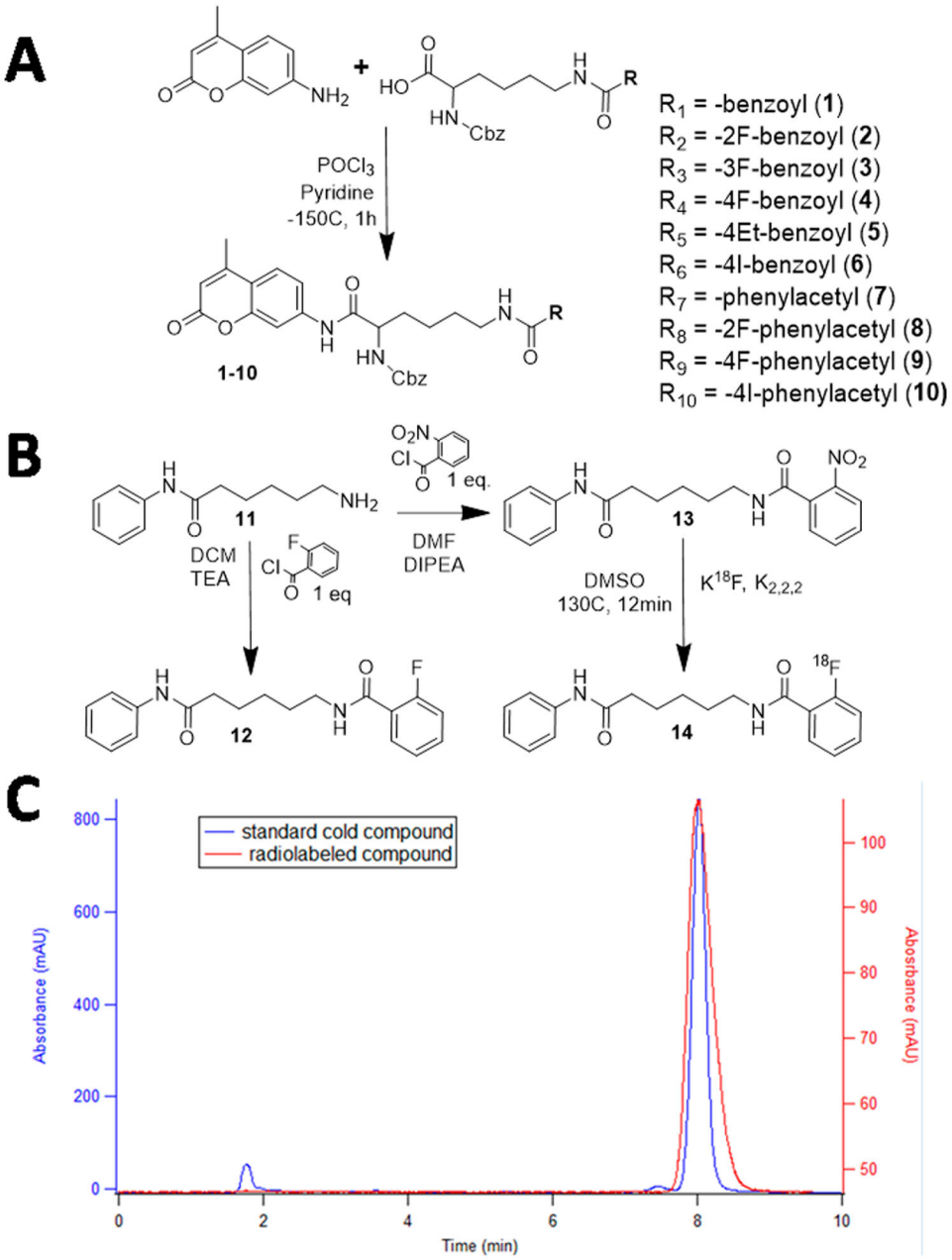

Figure 1.

(A) Chemical synthesis of compounds **1**−**10** using the Cbz-Lys-AMC backbone. (B) Synthesis of 2-FBzAHA (12) and precursor 2-NO_2BzAHA (**13**) and radiosynthesis of 2-[^{18}F]BzAHA (**14**) from the aminohexanoicanilide backbone. (C) Quality-control chromatogram demonstrating matching elution times for both the standard compound, **12** (blue), and the radiofluorinated compound, **14** (2-[^{18}F]BzAHA, red).

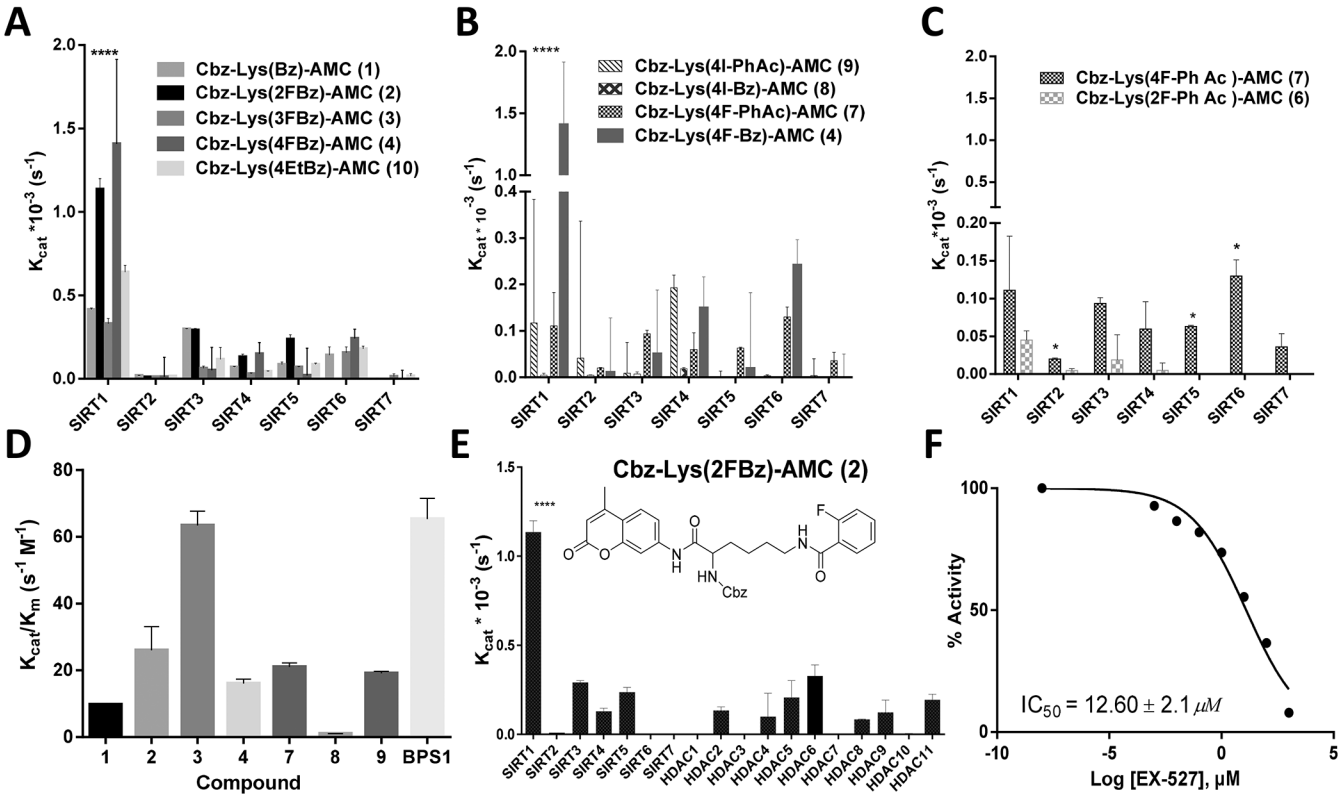

Figure 2.

(A−C) Catalytic efficacy (K_{cat}, s^{-1}) of compounds **1−10** with SIRT1−7 as determined by an enzymatic assay with a fluorescent readout. (A) Compounds **1−4** and **10** demonstrating differences in K_{cat} as a result of aromatic substitution of the fluorine atom at varying positions on the benzoyl moiety or the addition of a bulkier ethyl group. (B) Variations in K_{cat} due to the use of either a benzoyl or phenylacetyl moiety with para positioning of iodine or fluorine, demonstrating a significant increase with para-fluorobenzoyl (**4**) as compared with those of the others. (C) Comparison of *ortho*- and *para*-fluorine substitutions (**6** vs **7**) on the aromatic ring of a phenylacetyl moiety. (D) Catalytic efficacy (K_{cat}/K_m, s^{-1} M^{-1}) of selected compounds with recombinant SIRT1, as determined by a fluorometric assay, demonstrating that 2 is cleaved most efficiently by SIRT1. (E) Compound **2** selectively cleaved by SIRT1 with at least 3-fold greater efficacy as compared with by SIRT2−7 and HDAC1−11. (F) SIRT1 cleavage of **2** with increasing levels of EX-527, a selective SIRT1 inhibitor (IC_{50} = 12.60 ± 2.1 μM). Error bars represent standard deviations. All experiments were performed in triplicate. ****$P < 0.01$, *$P < 0.05$.

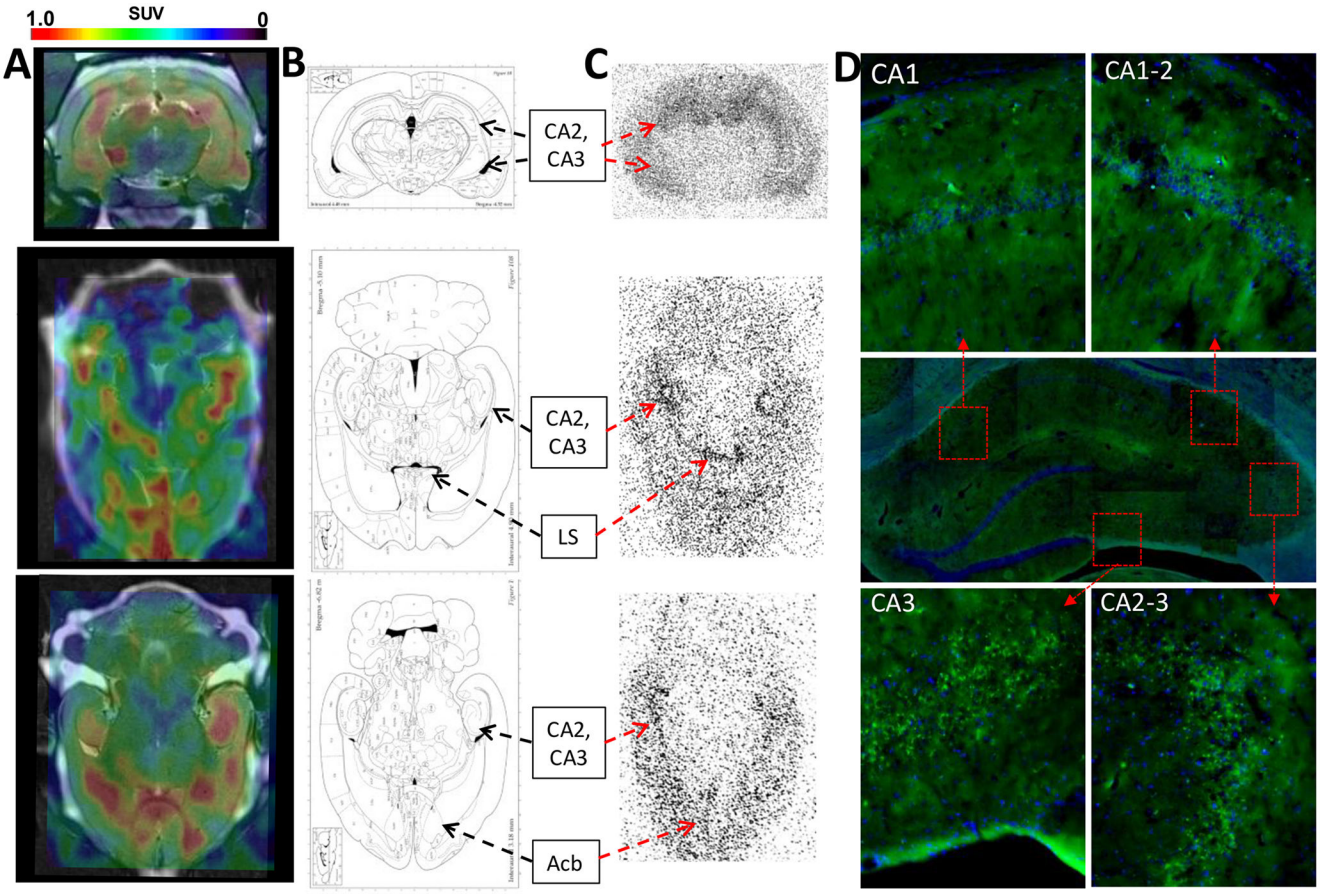

Figure 3.

(A) PET−CT−MR coronal and axial images 20 min after iv administration of 2-[^{18}F]BzAHA, demonstrating increased 2-[^{18}F]BzAHA-derived accumulation within regions of the brain corresponding to the hippocampus (CA1−CA3), lateral septal nucleus (LS), and nucleus accumbens (Acb). (B) Maps of the brain corresponding to the PET images. (C) Autoradiography performed for matching sections of the brain at 20 min after iv administration of 2-[^{18}F]BzAHA demonstrating increased radioactivity within regions of the hippocampus, nucleus accumbens, and lateral septal nucleus. (D) Immunofluorescence of corresponding slices of the brain demonstrated increased levels of SIRT1 expression in the hippocampus (Alexafluor488-conjugated anti-SIRT1, green), especially CA2 and CA3, overlaid on DAPI nuclear stain (blue).

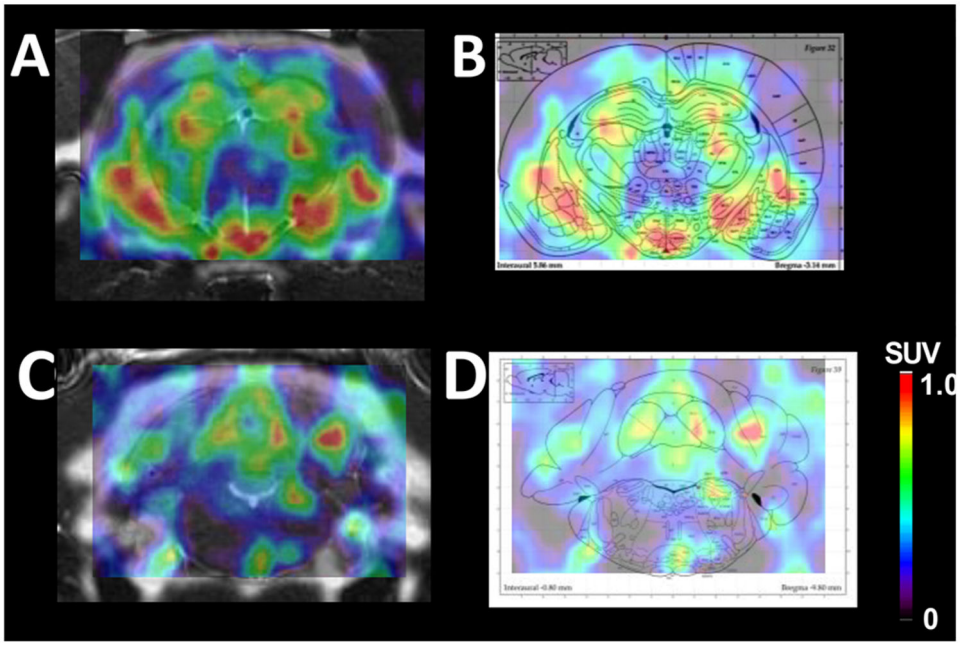

Figure 4.

(A) PET−CT−MR image of the hypothalamus taken at 20 min after iv administration of 2-[^{18}F]BzAHA. (B) PET image overlaid on an atlas map of the corresponding brain region demonstrating the colocalization between areas of increased 2-[^{18}F]BzAHA-derived radioactivity and the hypothalamus region as shown on the map. (C) PET−CT−MR image demonstrating increased 2-[^{18}F]BzAHA-derived accumulation within regions of the locus coeruleus. (D) PET image overlaid on the atlas map of the corresponding brain region, demonstrating colocalization between areas of increased 2-[^{18}F]BzAHA-derived radioactivity and the locus coeruleus region as shown on the map.

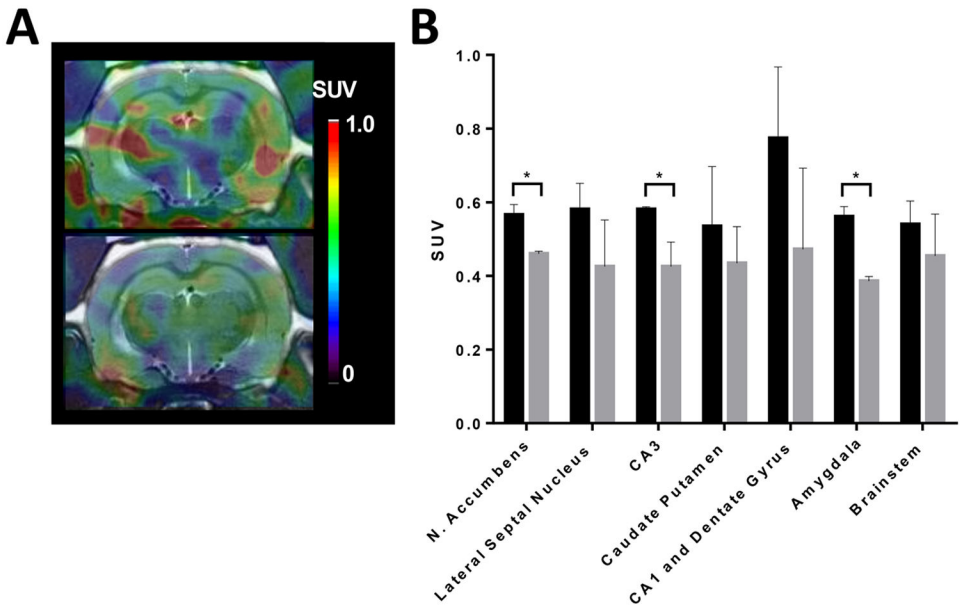

Figure 5.

(A) PET−CT−MR images at 20 min after iv administration of 2-[^{18}F]BzAHA. (B) PET−CT−MR images at 20 min after iv administration of 2[^{18}F]BzAHA and 50 min after pretreatment with the SIRT1 selective inhibitor, EX-527 (ip; 5 mg/kg). (C) SUV values for the ROI at 20 min after iv administration of 2-[^{18}F]BzAHA with (gray) and without (black) pretreatment with EX-527. Error bars represent standard deviation ($n = 2$). *$P < 0.05$.